

Characterization of the Inner Knot of the Crab: The Site of the Gamma-ray Flares?

Alexander Rudy¹, Dieter Horns², Andrea DeLuca³, Jeffery Kolodziejczak⁴, Allyn Tennant⁴, Yajie Yuan⁷, Rolf Buehler⁵, Jonathon Arons⁶, Roger Blandford⁷, Patrizia Caraveo³, Enrico Costa⁸, Stephan Funk⁷, Elizabeth Hays¹¹, Andrei Lobanov⁷, Claire Max¹, Michael Mayer⁵, Roberto Mignani¹⁰, Stephen L. O'Dell⁴, Roger Romani⁷, Marco Tavani³, Martin C. Weisskopf⁴

ABSTRACT

One of the most intriguing results from the γ -ray instruments currently in orbit has been the detection of powerful flares from the Crab Nebula. Such events, with a cadence of about one per year, can be so dramatic as to make the system the brightest source in the γ -ray sky as occurred in 2011 April. These flares challenge our understanding of pulsar wind nebulae and models for particle acceleration. To pinpoint the production site(s) within the Nebula, a multiwavelength

¹Department of Astronomy & Astrophysics, University of California, Santa Cruz, CA 95064, USA

²Institut für Experimentalphysik, Universität Hamburg, Luruper Chaussee 149, D-22761 Hamburg, Germany

³INAF–IASF Milano, via E. Bassini 15, I-20133 Milano, Italy; INFN Pavia, via A. Bassi 6, I-27100 Pavia, Italy

⁴NASA Marshall Space Flight Center, Astrophysics Office (ZP12), Huntsville, AL 35812, USA

⁵DESY, Platanenallee 6, D-15738 Zeuthen, Germany

⁶Astronomy Department and Theoretical Astrophysics Center, University of California, Berkeley, 601 Campbell Hall, Berkeley, CA 94720, USA

⁷W. W. Hansen Experimental Physics Laboratory, Kavli Institute for Particle Astrophysics and Cosmology, Stanford University, Stanford, CA 94305, USA

⁸INFN Roma Tor Vergata, via della Ricerca Scientifica 1, I-00133 Roma, Italy

⁹Max-Planck-Institut für Radioastronomie, auf dem Hügel 69, D-53121 Bonn, Germany

¹⁰INAF–IASF Milano, via E. Bassini 15, I-20133 Milano, Italy; Kepler Institute of Astronomy, University of Zielona Gora, Lubuska 2, 65-265 Zielona Gora, Poland

¹¹NASA Goddard Space Flight Center, Astrophysics Science Division, Greenbelt, MD 20771, USA

campaign has been carried out using Keck, *Hubble Space Telescope* (HST), and *Chandra X-ray Observatory*. As the short time scales of the flares ($\lesssim 1$ day) suggest a small emitting region, the Crab’s inner knot, located within a fraction of an arcsecond from the pulsar, has been proposed to be just such a site. In this paper, we focus on IR, optical, and X-ray observations of this feature to see if it might be related to the γ -ray flares and to try to understand its nature. We find that the knot’s radial size, tangential size, peak flux, and the ratio of the knot flux to that of the pulsar as measured with HST are all correlated with the projected distance of the knot from the pulsar. A new approach, using singular value decomposition for analyzing time series of images, was introduced yielding results consistent with the more traditional methods while some uncertainties were substantially reduced.

We exploit the new characterization of the Crab’s inner knot to discuss constraints on standard shock-model parameters that may be inferred from our observations assuming the inner knot lies near to the shocked surface. These include inferences as to wind magnetization σ , shock shape parameters such as incident angle δ_1 and poloidal radius of curvature R_c , as well as the IR/optical emitting particle enthalpy fraction. We find that while the standard shock model gives good agreement with observation in many respects, there remain two puzzles: (a) the observed angular size of the knot relative to the pulsar–knot separation is measured to be much smaller than expected; (b) the variable, yet high degree of polarization reported is difficult to reconcile with a highly relativistic downstream flow. In contrast, the IR/optical flux of the inner knot is marginally consistent with the scenario that the shock accelerates most of the optical emitting particles in the nebula.

Subject headings: neutron stars: general — pulsars: individual — Crab nebula and pulsar (PSR B0531+21) — inner knot

1. Introduction

The Crab pulsar and its nebula are one of the most studied targets in the sky at all wavelengths. It serves as a test bed for pulsar theories as well as, more generally, for astrophysical non-thermal processes. A very thorough review of the Crab system, including high spatial resolution observations with HST and *Chandra*, showing the complex, dynamic interaction of the pulsar wind with the surrounding medium, has been compiled by Hester (2008). A more recent review by Bühler & Blandford (2014) also includes the saga of the

γ -ray flares.

A crucial question implied by the observations of the γ -ray flares is “how are the particles being accelerated to sustain the flaring behavior?” Radiating particles must have PeV energies to emit synchrotron radiation at the observed γ -ray wavelengths. A mechanism is needed that can accelerate particles to such high energies in less than one gyration time in the ambient magnetic field. For example, the large flare of 2011 April produced a radiant energy equivalent to the energy stored in the mean magnetic field within a region of order 2×10^{14} m subtending an angle $\approx 0.3''$ at 2 kpc, consistent with the emission-region size estimated from light-travel-time arguments (Weisskopf et al. 2013).

An intense theoretical effort is currently being devoted to explain the variable Crab behavior (e.g., Uzdensky et al. 2011; Yuan et al. 2011; Komissarov & Lyutikov 2011; Arons 2012; Sturrock & Aschwanden 2012; Lyubarsky 2012; Lyutikov et al. 2012; Bykov et al. 2012; Clausen-Brown & Lyutikov 2012; Cerutti et al. 2012, 2013; Baty et al. 2013; Teraki & Takahara 2013). However, the mechanism driving the flares, their impulsive nature, the ≈ 12 -month recurrence time, and the location, remain unknown. Possible explanations include plasma instabilities in the nebula, magnetic reconnection, discontinuity in the pulsar wind acceleration, emission from the anvil, emission from the inner knot, or portions of the termination shock. See, for example, the review by Hester (2008) for the association of specific features with this nomenclature

There are a number of reasons to suspect that the feature known as the “inner knot” should be considered as a possible site for the origin of the flares (e.g., Komissarov & Lyutikov 2011). First, the luminosity of the flares accounts for a relatively high fraction of the pulsar spin-down luminosity (assuming a radiation efficiency of 3–5%), suggesting an origin in a region close to the pulsar (Tavani et al. 2011). Second, the very short variability time scales combined with causality arguments, strongly constrain the size of the flare’s emitting region (Buehler et al. 2012; Striani et al. 2011).

A multiwavelength campaign to study the Crab, described in Weisskopf et al. (2013), is being performed. Another γ -ray flare—the second largest observed to date—was detected with *Fermi*/LAT in 2013 March (Mayer et al. 2013). This triggered further observations with Keck, with the *Hubble Space Telescope* (HST), and with the *Chandra X-ray Observatory*. Here we concentrate on what was learned about the inner knot as a consequence of this campaign. We note that very-high-energy ($E \geq 100$ GeV) contemporaneous data from the HESS (H. E. S. S. Collaboration et al. 2014) and VERITAS (Aliu et al. 2014) Cherenkov-telescope arrays found no significant correlation of TeV flux with the flare observed with *Fermi*/LAT.

The observations are presented in §2. The measured properties of the knot are given in §3. §4 compares observations of the inner knot at the different wavelengths. Comparison and examination of possible correlations of the knot’s properties with γ -rays detected using the *Fermi*/LAT are discussed in §5. §6 discusses theoretical implications. §7 summarizes.

2. The Observations

The feature we refer to as the “inner knot” (aka “knot 1”, or “synchrotron knot”) was discovered by Hester et al. (1995) in a detailed study of the Crab using high-resolution images taken with HST. The feature, although resolved in those data, is small ($\approx 0.1''$) and close to the pulsar ($\approx 0.6''$). The feature was first suggested to be associated with a shock or instability in the jet ≈ 1500 AU from the pulsar, due to its good alignment with the jet and elongation perpendicular to the jet. Later Komissarov & Lyubarsky (2003) proposed, based on two-dimensional magnetohydrodynamic (MHD) simulation of the pulsar wind nebula, that the knot represents Doppler-boosted emission from an oblique termination shock. Synthetic synchrotron images from these 2D simulations (Komissarov & Lyutikov 2011) and more recently 3D simulations (Porth et al. 2014) indeed show a knot-like feature when the system is viewed from the proper (and reasonable) orientation. Moreover, the observed high degree of polarization and a position angle aligned with the symmetry axis (Moran et al. 2013) seems to lend further support to the oblique-shock scenario.

The salient features of the inner knot deduced prior to our observations are that it has a power-law spectrum $F_\nu \propto \nu^{-\alpha}$ with index $\alpha \sim 0.8$ in the IR to optical (Sollerman (2003), Melatos et al. (2005)) and, as most recently measured by Moran et al. (2013), the flux varies, the position appears to change, the degree of polarization is very large but does not appear to change with the flux (but see the discussion at the end of §5), and the magnetic field (determined from the position angle of the optical polarization) is orthogonal to the axis of symmetry (presumably the spin axis) and consistent with the direction of the field for the rest of the inner nebula.

2.1. Keck

We obtained K’ and H band near-infrared (NIR) images of the inner $40''$ of the Crab Nebula using the Keck Near-Infrared Camera 2 (NIRC2; K. Matthews, PI), with laser-guide-star adaptive optics (AO; Wizinowich et al. 2006). From 2012 February to 2014 January, we obtained 11 observations of the nebula during γ -ray quiescent periods and 1 target-

of-opportunity observation (K8) triggered by γ -ray flares. Table 1 summarizes the Keck observations.

Data reduction was carried out using the pipeline developed by Ghez et al. (2008). Individual frames were sky-subtracted, flat-fielded, bad-pixel-corrected, and corrected for the NIRC2’s camera distortion. We used the solution developed by Yelda et al. (2010), which matched the positions of stars in the globular cluster M92 measured with HST to those measured in the NIRC2. Frames were checked to ensure that they showed no irregularities in the point-spread function (PSF), and that the Strehl ratio was at least ~ 0.10 . Individual frames were then combined using the Drizzle algorithm (Fruchter & Hook 2002) to provide sub-pixel accuracy and high signal-to-noise images for analysis and modeling (§3.1 and Appendix).

The observations were conducted with two different pixel scales, using the NIRC2 “wide” camera, with $0.04''$ pixels and a $40'' \times 40''$ field of view, and the NIRC2 “narrow” camera, with $0.01''$ pixels and a $10'' \times 10''$ field of view. The total effective exposure times ranged from 420 to ≈ 2600 seconds. The shorter exposures result in optimal use of 1-hour Target-of-Opportunity interrupts—including acquisition, calibration, and sky measurements.

The spatial resolution of Keck’s NIRC2 with AO proved to be very effective in resolving the detailed structure and position of the knot. Figure 1 shows the 12 NIRC2 images. In the narrow camera, the center of the pulsar and the center of the knot are separated by ≈ 60 pixels. Typical values for the signal-to-noise ratio of the knot are 5. The PSF of NIRC2 with AO varies slightly in time due to the variable performance of the AO system. As the pulsar and knot are well resolved from each other in the Keck images, we chose not to deconvolve the PSF from the Keck images.

2.2. HST

Since 2012 January, we have obtained 17 observations using the HST Advanced Camera for Surveys (ACS) Wide-Field Channel (WFC), with $0.05''$ pixels. Each observation comprises 4 exposures totaling 2000 seconds and uses a standard 4-point BOX dithering pattern to fill the inter-chip gap as well as to allow efficient cosmic-ray cleaning. We employed the F550M filter, which is well suited to sampling continuum emission from the Crab with almost no contamination from line emission.

Table 2 summarizes the observations, listing the date and the mean observing time. The Appendix discusses in detail our analyses of the 17 HST/ACS images. Figure 2 displays the processed images, which have removed effects of the HST/ACS WFC point spread function

using singular-value decomposition (SVD) and Richardson-Lucy deconvolution.

2.3. *Chandra*

Our approach for searching for X-ray emission from the inner knot with *Chandra* involved a special use of both the high time resolution and high spatial resolution of the High-Resolution Camera for Spectroscopy (HRC-S) array in timing mode. So doing combines the best spatial resolution and the best time resolution afforded by the *Chandra* instrumentation. To achieve the time resolution, it is vital that the counting rate be below the rate where telemetry is saturated (see, e.g., Tennant et al. 2001). Consequently, the Low-Energy Transmission Grating (LETG) was inserted into the optical path to reduce the flux. As inserting the grating is of itself insufficient to avoid telemetry saturation, the trigger threshold of the HRC-S was raised to reduce the rate of detected events. This approach was first successfully used in a trial experiment (ObsID 11245) on 2010 November 16.

The next set of observations in this mode was initiated by us on 2013 March 5 as part of a sequence triggered by a γ -ray flare (Ojha et al. 2013). Unfortunately, the gain of the HRC had dropped since 2010. Consequently, the trigger threshold was too high during our first observation on March 5-6, reducing the counting rate from the pulsar to about a quarter of that expected, dramatically decreasing the number of detected counts. The next HRC observation was to take place on March 10 and the observation had already been fully planned with the commands to execute onboard the spacecraft. To replan at this stage would require an extremely short turnaround, yet it was accomplished. Finally, beginning on 2013 October 22, we triggered another sequence of HRC observations in response to the announcement of another γ -ray flare (Buson et al. 2013).

We also consider ObsID 9765 taken on 2008 January 22. For this observation the HRC was operated in a more standard configuration with the threshold set at the nominal value. However, to reduce the count rate, a blade was inserted into the optical path, which is no longer allowed. This blade also reduced the diffracted flux in one direction. By chance, this reduction is greatest near the nominal location of the knot. This reduction, together with a long integration time for this observation, results in ObsID 9765 providing the best data for study of the knot. Table 3 summarizes the relevant *Chandra* observations.

3. Properties of the Knot

3.1. Keck

Table 4 lists the best-fit values of the model parameters for the inner knot for each of the 12 Keck observations based upon the analysis and modeling described in the Appendix. The properties are these: ψ_0 , the position angle (E of N) from the pulsar to the center of the knot; r_0 , the projected separation between the pulsar and the knot; FWHM_r , the full width at half maximum of the knot in the radial direction; FWHM_t , the FWHM of the knot in the tangential direction; and F_k/F_p , the ratio of the flux in the knot to that in the pulsar. The flux ratio is used as measuring the fluxes of the 5 stars in in the NIRC2-wide camera’s field of view shows that those fluxes change relative to each other from one observation to the next. This occurs because the nebular background varies spatially across the detector in a non-trivial way, making it difficult to determine precisely the flux of any given source. Consequently, we measure the ratio of the knot’s flux to the pulsar’s, rather than the knot’s absolute flux. Figure 3 plots these properties versus the pulsar–knot separation, based upon the Keck data.

We seek possible correlations of these properties with the separation r_0 from the pulsar, of the following form: $p(r_0) = p(r_1)[r_0/r_1]^q$. We choose a reference distance $r_1 = 0.6692''$, obtained from the logarithmic average of the 12 values of r_0 . The position angle of the knot, ψ_0 , was fit to the linear regression $\psi_0 = \psi_0(r_1) + \psi'_0(r_1)[r_0 - r_1]$. Table 5 tabulates the results of the regression analyses of the inner knots intrinsic properties with its (projected) separation from the pulsar. Based upon the F-test probability, the power-law regression analysis finds marginally significant correlations of the radial width, tangential width, and peak intensity (surface brightness) with separation. The correlation of the knot’s flux to the separation is not significant.

3.2. HST

Table 6 lists the best-fit values of the model parameters for the inner knot for each of the 17 HST observations based upon the modeling and analysis described in the Appendix. The properties are these: the position angle ψ_0 of the knot with respect to the pulsar, the (projected) distance r_0 from the pulsar, radial width (FWHM_r) and tangential width (FWHM_t) of the knot, the peak surface brightness S_k , the knot flux F_k , the pulsar flux, F_p , and flux ratio F_k/F_p . Although we expected the pulsar flux to be steady, we measured a small (2.5σ) variation. Consequently, we prefer to work with the flux ratio F_k/F_p .

In the Appendix we discuss two ways of analyzing these data. Table 6 presents the results for one of these methods. However, our general conclusions concerning the knot’s optical properties are for the most part the same for either analysis. Figure 4 plots the knot properties versus the pulsar–knot separation, based upon the HST data.

As with the Keck data, we perform a regression analysis of the inner knots intrinsic properties with its (projected) separation from the pulsar (Table 7). We choose a reference distance $r_1 = 0.6559''$, obtained from the logarithmic average of the 17 measured values of r_0 . The position angle of the knot, ψ_0 , was fit to a linear regression $\psi_0 = \psi_0(r_1) + \psi'_0(r_1)[r_0 - r_1]$.

Based upon the F-test probability, the power-law regression analysis finds statistically significant correlations of the tangential and radial widths with separation from the pulsar, as well as the previously known (Moran et al. 2013) anti-correlations of flux and peak surface brightness with separation. The correlation of ψ_0 with separation r_0 is the least strong. There is a small systematic bias in the power-law index of the FWHM_r correlation, in that the radial width of the knot at times approaches the resolution limit of the instrument and analysis procedures. Applying our analysis procedures (see Appendix) to simulated knots of known true radial width, we estimate that the smallest measured values of FWHM_r are oversized by about 7% and the largest by about 3%, which would increase the power-law index for the FWHM_r – r_0 correlation from $q = 0.72$ to about 0.8. Finally, we emphasize that we find similarly strong correlations—except for the flux—using the more traditional HST analysis methods described in the Appendix.

3.3. *Chandra*

For the *Chandra* data, the main question is whether X-ray emission from the knot can be detected—especially in the vicinity of the bright, X-ray-emitting pulsar. The answer, unfortunately, is “No” and here we set an informative upper limit to the X-ray flux of the inner knot relative to that of the pulsar.

Table 8 shows the number of counts in each of three extraction regions: (1) centered on the approximate location of the optical knot, (2) centered on the pulsar, and (3) placed on a reference region to estimate the background. Details may be found in the Appendix and are illustrated in Figure 5. The analysis was performed both for the full phase-averaged data and for the data at pulse minimum. Consider, for example, the phase-averaged data for ObsID 11245. Comparing the inner knot counts to the background (Table 8) we find an excess of 167 counts. If the excess were really due to the knot, we would accordingly expect an excess of 50 ($= 167 \times 0.3$) counts at phase minimum. As this was not the case, we

attribute the excess to the wings of the PSF from the pulsar and posit that it is due to the spring/fall asymmetry discussed in the Appendix. As the impact of that asymmetry is below the statistical noise for the data taken at phase minimum, we then use the phase-minimum data to derive upper limits. We convert our phase-minimum upper limit into a phase-average upper limit by accounting for the 0.3 phase duration of the minimum and then divide by the phase average pulsar flux. Results are listed in the last column in Table 8.

4. Comparison amongst observations of the inner knot

Our *Chandra* observations were unable to detect X-ray flux from the knot, setting a 3-sigma upper limit to the ratio of knot flux to pulsar flux $F_k/F_p < 0.0022$. This upper limit is 20–40 times smaller than the ratio measured in the optical ($F_k/F_p = 0.044 \pm 0.001$) and in the near-IR ($F_k/F_p = 0.079 \pm 0.005$), indicating that the optical–X-ray spectral index of the knot is significantly steeper (by at least 0.5) than that of the pulsar.

Both our infrared and optical observations detected time variability in the pulsar–knot separation, with roughly consistent separations when measured contemporaneously (see the lower portion of Figure 6). Correlations of knot properties with pulsar–knot separation are very strong for the optical measurements but rather weak for the infrared measurements. We attribute this difference to a combination of factors—including poorer statistics for the much shorter NIR measurements and a number of systematic effects, resulting in part from the NIR PSF and background varying across the field and in time. As the lower portion of Figure 6 and Table 4 indicate, NIR-measured separations at essentially the same epoch exhibit a scatter substantially larger than the quoted statistical errors in the measurement, thus suggesting the presence of unaccounted systematic errors.

5. Comparison with γ -ray fluxes

It is clear from the previous sections that the intrinsic properties of the optical knot are correlated with its projected separation from the pulsar. The correlation for the NIR knot is but marginally significant. Thus, in searching for any relationship between the knot and the γ -ray flux, we concentrate on the separation versus γ -ray flux. The analysis performed to reduce the *Fermi*/LAT data is the same as described in Mayer et al. (2013).

Table 9 lists the dates and separations measured in the Keck and in the HST observations, followed by the corresponding 12-hour-average *Fermi*/LAT ≥ 100 -MeV fluxes. The upper portion of Figure 6 shows the *Fermi*/LAT flux as a function of time covering the inter-

val when our Keck and HST observations were made. The vertical lines identify times when observations were made with Keck (red) or with HST (green). The lower portion of Figure 6 plots the pulsar–knot separations on the same time scale. Figure 7 expands Figure 6 at the times of the largest γ -ray flares.

Figure 8 plots the γ -ray flux versus the measured radial separation of the knot from the pulsar. The results captured in this figure clearly do not represent a significant simple correlation of the knot properties with the γ -ray flux: The formal correlation coefficient is only 0.2.

Inspection of the γ -ray light curve and the time series of pulsar–knot separations (Figure 6) indicates that the most energetic γ -ray flares occurred at a time which is not precisely coincident with the time of greatest pulsar–knot separation. It is reasonable to ask how probable such a coincidence would be as a chance occurrence. A simple answer is that the probability of a chance coincidence is just the difference in the central times of the two events divided by the total duration of this observing program, as described below.

We next estimate the time and duration of a γ -ray flare and the excursion in r_0 (lower portion of Figure 6), using a simple Gaussian model in both cases and including a linear baseline trend for the γ -ray flare. This is not to suggest that a Gaussian properly describes the underlying physical processes, but simply to enable comparison of the two time series, one for the flares, one for the separations. Fitting separation data in the MJD range 56180-56400 and γ -ray fluxes in the range 56345-56370 places the midpoint of the inner knot excursion at 56331.8, followed by the γ -ray flare at 56357.3, 25.5 days later. The Gaussian width is a measure of the event duration with FWHMs of 70.7 and 7.6 days for the separation excursion and γ -ray flare data respectively.

The time between our first and last pulsar–knot separation measurements is 826.1 days. However, on 4 occasions the gap between separation measurements was longer than the 70.7 day duration of the observed separation excursion. We assume then that a separation excursion would be observable if an observation fell within the FWHM window and not observable if it fell outside the window. To obtain the total observing program under this assumption, we remove the time of 4 gaps (140.1 days) that exceeded 70.7 days making the total duration of the observing program 686 days. Thus an estimate of the chance probability is $25.5/686 = 3.7\%$, which is approximately at the 2σ level.

It is worth noting that the largest pulsar–knot separation incursion (toward the pulsar) occurs near the second most energetic γ -ray flare. However, the knot separation data are sparser at this time. Therefore, we use the previous FWHM value of 70.7 days to establish the time of the incursion. With this prior, fitting the separation data in the MJD range

56390-56670 and γ -ray fluxes in the range 56575-56590 places the midpoint of the inner knot excursion at 56566.0, followed by the γ -ray flare at 56582.6, 16.6 days later.

In this second case, the comparable chance probability estimate is $16.6/686 = 2.4\%$ ($\sim 2.5\sigma$). As each variation of the knot-pulsar separation is of the opposite sign, we must multiply the probabilities by a factor of 2 when combining them. So our estimate of the chance probability that the 2 largest knot excursions/incursions would occur within the observed intervals of the 2 largest γ -ray flares is $0.037 \times 0.024 \times 4 = 0.4\%$, which is approximately at the 2.9σ level. There are additional γ -ray flares; however, the third most energetic flare occurs only 12 days later than the one on MJD 56582.6 and therefore is well within the assumed 70-day range of the associated knot incursion. The other flares are significantly weaker and less well-sampled by the optical/infrared observations.

Although coverage is sparse, there is no compelling evidence in the pulsar–knot separations for large ($> 0.01''$) excursions from the mean separation at time-scales comparable to the flare durations. Indeed, knot incursion/excursion time scales appear to be $> 10\times$ longer than flare durations, so direct correlation of the γ -ray light curve with the separation time-evolution produces correlation coefficients that are rather difficult to interpret without associated simulations. Such simulations would require assumptions regarding an underlying physical model relating the two curves. As we have no such model, any correlation analysis would be purely *ad hoc*.

The 0.4% value for the chance probability is based upon a rather simplistic analysis involving only 2 flares and was, of course, determined *a posteriori*. However, in continuing to monitor the Crab at multiple wavelengths with the goal of understanding the origin of its γ -ray flares, the inner knot will continue to be a feature of interest. Based upon the r_0 time scale of 71 days (30-day Gaussian 1σ), a monitoring program which includes monthly optical observations is necessary to detect significant inner-knot excursions from its mean pulsar separation. Monitoring every ~ 3 weeks should be sufficient to characterize fully these variations and to verify the small statistical sample from which these parameter estimates were derived.

We also note that an inner-knot incursion with an ≈ 2 -month FWHM timescale and $0.075'' \pm 0.025''$ pulsar–knot separation inward amplitude was also reported by Moran et al. (2013). This event appears to be quite similar in duration and amplitude to our observations. The reference also reports an $\approx 2\sigma$ apparent change in the knot polarization parameters, which occurred 22 ± 5 days after the time of maximum incursion. The degree of linear polarization steps from $59.9\% \pm 6.9\%$ on 2005 Nov 25 to $42.8\% \pm 6.2\%$ 2005 Dec 5 and the position angle changes from $125.4^\circ \pm 3.3^\circ$ to $121.6^\circ \pm 4.2^\circ$. Interestingly, the time frame of this polarization shift occurred in a window closely matching both the 25.5 and 16.6 day γ -

ray flare delays after the peak inner-knot excursion/incursion times discussed above. While the claimed 2σ result is not very significant, we observe that prior to the step near the start of 2005 December, all 10 of the reported measurements of the degree of linear polarization fall into a population with mean 60.7% and small standard deviation 1.0%, whereas the 2 subsequent measurements had a mean of 43.4% with standard deviation of 0.8%. If we suppose that the quoted errors in the reference apply to the absolute, but not relative measured values, then the size of the step change would be $> 10\sigma$ instead of $\approx 2\sigma$. This may be a reasonable assumption, as the point-to-point measurement variations are smaller by a factor > 6 than the quoted errors. Similar arguments would apply to the polarization position angle. From this we conclude that polarization should also be of interest in future attempts to relate inner-knot behavior to γ -ray flaring.

6. Implications for Theoretical Models

In the basic model of the Crab Nebula (e.g., Rees & Gunn 1974), the pulsar wind passes through a shock at a radius $\sim 3 \times 10^{17}$ cm where the wind momentum flux balances the nebular pressure. However, the wind should be anisotropic. For example, the momentum flux in a split-monopole $\propto \sin^2 \theta$ (Bogovalov 1999) and recent simulations suggest $\propto \sin^4 \theta$ (Tchekhovskoy et al. 2013; Tchekhovskoy, Philippov, & Spitkovsky 2015) where θ is the polar angle. As a result, the shock is likely to be quite oblate. The sections of the shock near the poles would be oblique and much closer to the pulsar than the equatorial part. The observed radiation presumably comes from relativistic particles (electrons or positrons) accelerated behind the shock. Since the outflow from an oblique shock can remain relativistic, we would be able to see a compact, emitting feature (the inner knot) if the relativistic outflow happens to be aligned with our line of sight so that its emission is beamed. The inner knot should appear to us as having some offset from the pulsar due to the deflection of the outflow from its presumed radial motion (Figure 9). If the shock is approximately axisymmetric as one would expect, the projected emitting site would fall on the projected symmetry axis, leading to an alignment with the jet. The shape of the inner knot should also be more or less symmetric about the axis; whether it is elongated parallel or perpendicular to the axis depends on the geometry of the oblique shock. Furthermore the synchrotron emission should be linearly polarized (Komissarov & Lyutikov 2011, Yuan & Blandford 2015 in preparation).

The shock model predicts that the scaling between the observed properties of the knot—projected pulsar–knot separation r_0 , tangential angular width FWHM_t , radial angular width FWHM_r and surface brightness S_k —should be determined by the upstream magnetization $\sigma \equiv B_1^2 / \mu_0 n_1 \gamma_1^2 m c^2$ (where m is electron mass and B_1, n_1, γ_1 are upstream magnetic field,

proper density, bulk Lorentz factor, respectively) plus three more parameters that characterize the shape of the shock near the emitting site: The unprojected pulsar-knot separation r_k ; the incident angle δ_1 , defined to be the angle between upstream velocity and the shock surface as shown in Figure 9; and the shock poloidal radius of curvature R_c .

Let the outflow be deflected from the radial direction by an angle Δ at the shock. We then have $r_0 = r_k \Delta$. The knot tangential size is determined by the Doppler beaming and the shock radius of curvature in the toroidal direction as $\text{FWHM}_t \approx 2r_k/\gamma$, where γ is the downstream Lorentz factor. In the simplest shock model with an isotropic plasma, both Δ and γ are functions of σ and δ_1 : $\Delta = \delta_1 - \arctan(\chi \tan \delta_1)$ and $\gamma = 1/(\sin \delta_1 \sqrt{1 - \chi^2})$, where $\chi \equiv v_{2\perp}/v_{1\perp} = B_1/B_2 = (1 + 2\sigma + \sqrt{16\sigma^2 + 16\sigma + 1})/6(1 + \sigma)$ is the compression ratio at the shock, $v_{1,2\perp}$ being the component of upstream/downstream velocity perpendicular to the shock (Komissarov & Lyutikov 2011). The radial knot size FWHM_r should also be proportional to r_k/γ but will have an additional factor involving the ratio R_c/r_k .

As to the intensity, we assume that the emitting particles have a power-law distribution $\propto n'\gamma'^{-p}$ in the fluid rest frame, where n' , γ' are particle density and Lorentz factor in the same reference frame, and $p \sim 2.6$ from the measured spectral index of the knot (Sollerman 2003; Melatos et al. 2005).

The emissivity in the fluid rest frame is $j'_{\nu'}(\nu') \propto n' B'^{(p+1)/2} \nu'^{-(p-1)/2}$, where B' and ν' are magnetic field and radiation frequency measured in this reference frame. After transforming to the nebula frame, the emissivity has a dependence on the flow Lorentz factor γ , particle (improper) number density n , and magnetic field B as follows: $j_\nu \propto \mathcal{D}^{2+(p-1)/2} (n/\gamma) (B/\gamma)^{(p+1)/2}$, where $\mathcal{D} = \nu/\nu' = \sqrt{1 - \beta^2}/(1 - \vec{\beta} \cdot \vec{n})$ is the Doppler factor, in which $\vec{\beta}$ is the flow velocity and \vec{n} is a unit vector along the direction of line of sight. The surface brightness corresponds to the emissivity integrated along the line of sight in the nebular frame: $S_\nu = \int j_\nu dl$. To estimate the peak surface brightness, one takes the maximum Doppler factor $\mathcal{D} \approx 2\gamma$, and we get $S_{\nu,peak} \propto n B^{(p+1)/2} \ell$ where ℓ is an estimation of the length of the emitting region along the line of sight. As roughly $B \propto r_k^{-1}$ and $n \propto r_k^{-2}$, we have $S_{\nu,peak} \propto r_k^{-2-(p+1)/2} \ell$.

These previous relations allow us to set the constraints discussed below using both the steady and variable properties of the knot.

6.1. Variability

In the shock model, variability can arise either upstream or downstream of the shock. Firstly, stress tensor variation in the nebula can cause the shock radius and shape to vary

over time. Three dimensional MHD simulations (Porth et al. 2014) show that even if the upstream condition is fixed, the post-shock flow can be quite variable: there is vortex-shedding from the termination shock, and the shock constantly interacts with waves and vortices in the nebula. Those variations are expected to be mostly magnetic in origin, and the interactions between the shock and the downstream flow are quite nonlinear. The picture is similar to earlier 2D simulations (e.g., Camus et al. 2009) except that the kink instability sets in so that the hoop compression is less prominent as in the 2D case; also short-term variability is less pronounced. The 3D simulations give a typical variation time scale of less than one year.

Now suppose that the change of downstream pressure causes the shock radius r_k to change. For simplicity we first assume that Δ , ℓ , γ and p stay more or less the same, then from the above scaling relations, we have $S_{\nu,peak} \propto r_0^{-2-(p+1)/2}$, $\text{FWHM}_t \propto r_0$, and knot flux $F_\nu \propto S_{\nu,peak} \text{FWHM}_t \text{FWHM}_r \propto r_0^{-(p+1)/2}$, assuming FWHM_r to be also roughly proportional to r_k . In reality Δ , ℓ , γ change with the shock radius r_k as well, as the shock shape and upstream incident angle δ_1 vary. Consequently, the observed correlation is more complicated and less clean; however, the general trend is consistent with our expectation of the shock model.

Variations initiated by the pulsar can also cause the knot properties to change. In such a scenario, the shortest possible variation time scale is $t_v \sim r_k(1 - \cos(1/\gamma))/c \sim r_k/(2\gamma^2 c) \sim 1 \text{ day}(r_k/10^{17} \text{ cm})(\gamma/5)^{-2}$ up to 10% inaccuracy assuming $\gamma \gtrsim 3$. However, there is no evidence in the pulsar timing that this is actually happening.

6.2. Time averaged properties of the knot

The properties of the knot may be used to set constraints on the flow composition and how much dissipation occurs at the shock. One constraint comes from geometrical relations amongst the three measured angles r_0 , FWHM_t , and FWHM_r . For the simplest shock model, we have $r_0 = r_k \Delta$ and $\text{FWHM}_t \approx r_k/\gamma$, where Δ and γ only depend on σ and δ_1 , such that the ratio FWHM_t/r_0 sets limit on σ and δ_1 . We find that $\text{FWHM}_t/r_0 = 2/(\gamma\Delta) = 2 \sin \delta_1 \sqrt{1 - \chi^2}/[\delta_1 - \arctan(\chi \tan \delta_1)] \geq 2.8$, with the minimum at $\sigma = 0$ and $\delta_1 = 0.39$. In contrast, the observation gives $\text{FWHM}_t \sim 0.5r_0$, indicating that some important ingredient is missing in the standard shock model. For example, the upstream flow might have already been bent before arriving at the shock; and/or the anisotropic particle distribution downstream might be important in determining the size of the knot. Although more detailed investigations will be described elsewhere, the above discussion on variability and the following discussion on energetics should be valid for quite general shock

models.

The shape of the knot also has some interesting implications. In both the *Hubble* and Keck images, the knot is not just a simple ellipse that only involves quadratic terms of coordinates; it has curvature and appears to be convex away from the pulsar (“smile”), so at least a third moment of the coordinates is needed to describe the shape. A simple intuitive picture is based on the geometry that the shock surface is similar to a torus centered on the pulsar and we look through the hole from the bottom. If emission from the shock outflow roughly follows the local toroidal magnetic field, one would imagine the knot to be convex toward the pulsar (“frown”)—contradictory to what we see. In fact, we should not overlook the possibility that the outflow may have significant bending downstream. If the outflow bends toward the equator by an angle $\sim 1/\gamma$ within the emission length, we would see the knot more extended (contracted) on the far (near) side with respect to the pulsar, as additional flow lines enter (originally aligned flow lines leave) the emission cone on the corresponding side.

Another constraint comes from the observed flux of the knot. In the K' band, the typical knot-pulsar flux ratio is ~ 0.063 (Table 4). If we take the photometry of the pulsar from Sandberg & Sollerman (2009), the pulsar K_s band magnitude is 13.80 ± 0.01 , after dereddening with the best fit value $E(B - V) = 0.52$ (Sollerman et al. 2000) and the extinction law from Fitzpatrick (1999), this corresponds to a flux of $2.2 \times 10^{-26} \text{erg s}^{-1} \text{cm}^{-2} \text{Hz}^{-1}$. So the inner knot flux in K' band should be roughly $F_\nu^{\text{knot}} = 1.4 \times 10^{-27} \text{erg s}^{-1} \text{cm}^{-2} \text{Hz}^{-1}$. Similarly, optical data (Table 6) on average give a dereddened flux of $F_\nu^{\text{knot}} = 1 \times 10^{-27} \text{erg s}^{-1} \text{cm}^{-2} \text{Hz}^{-1}$. However, we do not attempt here to get a spectral index using the time averaged fluxes due to the variability of the knot and the fact that most of the multi-wavelength observations are not simultaneous. Previous measurements by Sollerman (2003) and Melatos et al. (2005) indicate that the spectrum of the knot in IR to optical range is a power law $F_\nu \propto \nu^{-\alpha}$ with $\alpha \sim 0.8$, and Melatos et al. (2005) further measured that this power law extends to NUV (160 – 320 nm), with a flux in NUV $F_\nu^{\text{knot}} = 0.12 \text{ mJy} = 1.2 \times 10^{-27} \text{erg s}^{-1} \text{cm}^{-2} \text{Hz}^{-1}$ —this is the highest energy at which the knot has been measured. A few more recent measurements show slightly different spectral index ranging from 0.63 (Tziamtzis et al. 2009) to 1.3 (Sandberg & Sollerman 2009) but unfortunately these are based on non-simultaneous data. It would be very interesting to refine the spectral measurement using near simultaneous IR/optical images in the future. In what follows we adopt a fiducial spectral model $F_\nu^{\text{knot}} \sim 10^{-27} (\nu/10^{15} \text{ Hz})^{-0.8} \text{erg s}^{-1} \text{cm}^{-2} \text{Hz}^{-1}$ with the caveat that this could change with better observations.

Using the above spectral model, we find that the knot integrated flux in IR/optical band ($(0.1 - 2) \times 10^{15} \text{ Hz}$) is $F_{\text{O/IR}}^{\text{knot}} = 2.6 \times 10^{-12} \text{erg s}^{-1} \text{cm}^{-2}$. Thus, the luminosity of the knot

per steradian is $L_{O/IR,\Omega} = D^2 F_{O/IR}^{\text{knot}} = 10^{32} \text{ erg s}^{-1}$, where $D \sim 2 \text{ kpc}$ is the distance of the Crab. If we define $\epsilon \equiv L_{O/IR,\Omega}/(\dot{E}/4\pi)$, where $\dot{E} = 5 \times 10^{38} \text{ erg s}^{-1}$ is the pulsar spin-down power, ϵ can be used as a measure of the radiative efficiency of the shock along the direction of line of sight in IR to optical range. Here we find $\epsilon = 2.5 \times 10^{-6}$ and the shock is highly adiabatic.

We can get an estimation of the enthalpy fraction of IR/optical emitting particles in the downstream flow

$$\eta(\gamma') = \frac{8}{3} \frac{\gamma' t'_{\text{cool}}}{t_{\text{flow}}} \frac{\nu L_{\nu,\Omega}}{\dot{E}/(4\pi)} = \frac{8}{3} \frac{\gamma' t'_{\text{cool}}}{t_{\text{flow}}} \frac{\nu L_{\nu,\Omega}}{\dot{E}/(4\pi)}, \quad (1)$$

where t_{flow} is the flow time scale and $t'_{\text{cool}} = 6\pi\epsilon_0 m^3 c^3 / (e^4 B'^2 \gamma') \approx 10^2 \gamma^2 B_{-3}^{-3/2} \nu_{14}^{-1/2}$ years is the synchrotron cooling time of the particles in the fluid rest frame (we have adopted $B = B_{-3} \text{ mG}$ and $\nu = \nu_{14} 10^{14} \text{ Hz}$ for the numerical value). Thus the particle injection rate per unit steradian in corresponding energy band is

$$\dot{N}(\gamma') = \frac{3\eta(\gamma')}{4\gamma' m c^2} \frac{\dot{E}}{4\pi\gamma}. \quad (2)$$

Adopting typical values $\gamma = 5\gamma_5$, $t_{\text{flow}} = r_{17} 10^{17} \text{ cm}/c$, we find that for IR emitting particles, $\eta_{\text{IR}} = 0.05\gamma_5^3 B_{-3}^{-3/2} r_{17}^{-1}$, and $\dot{N}_{\text{IR}} = 2 \times 10^{36} \gamma_5^2 B_{-3}^{-1} r_{17}^{-1} \text{ s}^{-1} \text{ sr}^{-1}$. The spectral index of the knot indicates that the particle distribution powerlaw index should be $p \sim 2.6$, thus the IR emitting particles should comprise the majority of particle pressure downstream. From the above estimations, it seems that the particle injection rate at the shock is marginally consistent with the scenario that most of the IR/optical emitting particles are provided by the shock.

Regarding particle acceleration mechanisms, we notice that IR emitting particles usually go through $N = t_{\text{flow}} \nu_g$ Larmor orbits, where $\nu_g = \nu_B/\gamma'$ is the relativistic gyrofrequency—the cyclotron frequency (ν_B) divided by the electron’s Lorentz factor (γ'). Eliminating γ' in favor of the magnetic field (B) and observing frequency (ν), the number of orbits within the flow timescale is $N \approx 6 \times 10^4 B_{-3}^{3/2} r_{17} \nu_{14}^{-1/2}$. To allow sufficient time for acceleration mechanisms requiring instabilities or stochastic processes to operate, requires that $N \gg 1$. However, for particles emitting γ rays of energy 300 MeV, $N \lesssim 1$, thus requiring special acceleration mechanisms—if the emitting electrons are indeed accelerated at the shock.

One more constraint comes from the polarization of the knot. Most recent polarimetry performed by Moran et al. (2013) gives a high polarization degree $\sim 60\%$, with position angle aligned with the symmetry axis, indicating strongly a toroidal magnetic field. Here we need to be careful about the depolarization effect due to relativistic kinematics (Lyutikov et al.

2003). What happens then is that Lorentz transformation of the emission of a relativistic plasma from the comoving frame to the lab frame produces a rotation of the polarization vector. For a curved emitting surface, neighboring fluid elements have slightly different velocities, thus their polarization vectors experience different amounts of rotation. As one sums the contribution from the visible surface (this is essentially what we observe), the result is some degree of depolarization. We find that for the oblique shock in the Crab Nebula, under an ultrarelativistic approximation, the upper limit of polarization degree is similar to that in Lyutikov et al. (2003): 56.25% for particle spectral index $p = 3$ and 43.4% for $p = 2$. Thus, the observed high degree of polarization and its possible variation is highly constraining on theoretical models. It would be interesting to repeat this observation, especially with adaptive optics.

7. Conclusions

We have (1) introduced a new approach to analyzing time series of images; (2) discovered that key properties of the knot (radial width, tangential width, flux) are correlated with the time-variable separation between the knot and the pulsar; (3) shown that, with the available data, it is not possible to determine a strong correlation between the knot separation and the occurrence of γ -ray flares; (4) set an upper limit to the low-energy X-ray flux from the inner knot; (5) discussed the implications of our observations to set constraints on particular elements of the standard shock modeling of the relativistic outflow from the pulsar. These include inferences as to wind magnetization σ , shock shape parameters such as incident angle δ_1 and poloidal radius of curvature R_c , as well as the IR/optical emitting particle enthalpy fraction. We found that while the standard shock model gives good agreements with observations in many aspects, there remain two puzzles: (a) the angular size of the knot relative to the pulsar–knot separation is much smaller than expected; (b) the variable, yet high degree of polarization is difficult to reconcile with a highly relativistic outflow. We also found that the IR/optical flux of the inner knot is marginally consistent with the scenario that the shock accelerates most of the optical emitting particles in the nebula.

Acknowledgments The *Fermi* LAT Collaboration acknowledges generous ongoing support from a number of agencies and institutes that have supported both the development and the operation of the LAT as well as scientific data analysis. These include the National Aeronautics and Space Administration and the Department of Energy in the United States, the Commissariat à l’Energie Atomique and the Centre National de la Recherche Scientifique / Institut National de Physique Nucléaire et de Physique des Particules in France, the Agenzia Spaziale Italiana and the Istituto Nazionale di Fisica Nucleare in Italy, the Ministry of

Education, Culture, Sports, Science and Technology (MEXT), High Energy Accelerator Research Organization (KEK) and Japan Aerospace Exploration Agency (JAXA) in Japan, and the K. A. Wallenberg Foundation, the Swedish Research Council and the Swedish National Space Board in Sweden. Additional support for science analysis during operations phase is gratefully acknowledged from the Istituto Nazionale di Astrofisica and the Centre d’Etudes Spatiales in France. The research leading to these results has also received funding from the European Commission Seventh Framework Programme (FP7/2007-2013) under grant agreement n. 267251. Several of the authors would also like to acknowledge both funding and solid support from the *Chandra* X-ray Center and the *Hubble Space Telescope* Science Institute under a number of observing proposals: GO3-14054Z, GO3-14057Z, GO4-15058Z, GO4-15059Z, GO-13109, GO-13196, GO-13348

A. Appendix - Data Analysis

A.1. Keck

To study the knot using the high-resolution Keck adaptive-optics (AO) data, we characterize the region around the pulsar using an empirically measured point spread function and an analytical model of the knot geometry.

A.1.1. PSF Subtraction

We subtracted the PSF of the pulsar using a nearby PSF star (Figure 10). During our observations, the laser guide star, and so the center of the anisoplanatic patch, was aimed at the point half-way between the PSF star and the pulsar. We fit the PSF star, a background plus a power-law based seeing-disk to the pulsar. For the fit, we excluded the region in the pulsar subimage that surrounds the knot, and used the other 270°. The background was fit with a sloping plane model, to allow for the variable nebular background in the pulsar and PSF star subimages. The fitting was performed with a Levenburg-Marquadt fitter.

A.1.2. Deconvolution

We chose not to deconvolve the knot with the empirically measured point spread function. Tests on several images showed that deconvolution of the shape of the knot made insignificant differences to the fit values and uncertainty.

A.1.3. Knot Model

To fit the geometric parameters of the knot, we masked out the center diffraction-limited core of the pulsar, and used a Levenburg-Marquadt fitting technique to fit a two dimensional Gaussian to the shape of the Knot.

We used a model of the form

$$S(r, \psi) = S_b + S_k \exp(-\frac{1}{2}((r - r_0)^2/\sigma_r^2 + (\psi - \psi_0)^2/\sigma_\psi^2))$$

We also allowed the center of the coordinate system (x_0, y_0) to vary slightly (0.05"). To determine the fit uncertainties, we used the 1- σ errors from the self-covariance of the fit parameters. Results were tabulated in Table 4.

A.2. HST

A.2.1. HST - Traditional Analysis

In order to measure the knot properties (position, flux, tangential and radial width) we used the SExtractor package (Bertin & Arnouts 1996). SExtractor has been extensively used for the analysis of HST data, in particular for the ACS camera (e.g., for the *Hubble* Ultra Deep Field project, Beckwith et al. 2006). For source detection, we require a minimum of five contiguous pixels with a detection threshold 5σ above the root-mean-square (rms) background, with a total of 32 deblending subthresholds, and with a contrast parameter of 0.005, setting the background mesh size to 16×16 ACS pixels.

The position of a source is evaluated by SExtractor as the barycenter of the source brightness distribution. Flux is computed within an elliptical aperture, using an implementation of the method by Kron (1980). Note that the pulsar is not saturated and that diffraction spikes from the pulsar that might cross the inner knot only marginally affect its flux measurements. The parameters of this ellipse (semiaxes and orientation), evaluated using the second moments of the object's brightness distribution also yield a measure of the object morphology. Indeed, for the case of the knot, the direction of the minor axis of the ellipse turned out to be consistent with the pulsar-knot direction in all images. Thus, the minor axis and the major axis of the ellipse measure the RMS full widths (FWRMS) in the radial and tangential directions, respectively.

In order to assess systematic errors, we performed simulations with the ESO/MIDAS

software¹. We added to the ACS images a “synthetic knot”. To generate such an artificial source, we assumed a two-dimensional Gaussian brightness distribution, with the minor axis aligned with the true pulsar–knot direction. The synthetic knot was positioned to the NW of the pulsar, opposite but along the true pulsar–knot direction, and at an angular distance comparable to that of the true knot. We repeated the exercise by varying the flux, position, and morphology of the synthetic knot and we estimated the uncertainties in the parameters recovered using SExtractor²

Table 10 lists the best-fit values of the model parameters of the inner knot for each of the 17 observations based upon this traditional analysis and modeling. Table 11 shows the results of a regression analysis on the listed parameters.

A.2.2. HST Singular Value Decomposition (SVD)

As the inner knot is within 1'' of the Crab pulsar and varies in position and size, we also developed special procedures for characterizing it using the central 121×121 -pixel ($6.05'' \times 6.05''$) images of the 17 HST/ACS observations. The major steps are (1) to remove the pulsar from each image, (2) to use the residual image to generate an image of the inner knot, and (3) to characterize the properties of the inner knot.

Remove pulsar and generate an image.

In order to remove the pulsar from each of the 17 central 121×121 -pixel ($6.05'' \times 6.05''$) HST images, we first determine the PSF of the HST/ACS using 121×121 -pixel images around each of 19 isolated stars in the field. In doing this, we account for the fact that some observations were at a roll angle ~ 180 deg opposite that of the others. After subtracting a fitted linear gradient from the image of each (Figure 11) of the 19 stars and for each of the 17 observations, we register the resulting $323 = 19 \times 17$ star images and use singular-value decomposition (SVD) to generate a linear basis (lowest term shown in Figure 11) describing the PSF. The model pulsar image (Figure 11) uses the first 72 components of the SVD basis. After subtracting a linear gradient from each of the 17 central (pulsar) images (Figure 12), we fit each using the PSF basis to generate 17 residual (pulsar-removed) images (also Figure 12), each now dominated by the inner knot.

Characterize inner-knot properties.

¹ <https://www.eso.org/sci/software/esomidias/>

² <http://www.astromatic.net/software/sextractor>.

The measured extrinsic properties of the inner knot are the projected radial separation r_0 and polar angle ψ_0 of the peak surface brightness with respect to the pulsar. To facilitate characterization of the intrinsic properties of the inner knot, we map each inner-knot sub-image (Figure 12) onto a ψ - r grid (Figure 13). For an initial model of the surface brightness (intensity) distribution of the inner knot, we use a simple bivariate normal distribution: $S(r, \psi) = S_k \exp(-\frac{1}{2}((r - r_0)^2/\sigma_r^2 + (\psi - \psi_0)^2/\sigma_\psi^2))$.

The major intrinsic properties of the inner knot are its radial dispersion σ_r ($\text{FWHM}_r = 2.35\sigma_r$ for a Gaussian profile), azimuthal dispersion σ_ψ (or tangential dispersion $\sigma_t = r_0\sigma_\psi$), and peak intensity (surface brightness) S_k . Integrating the intensity over solid angle gives the flux $F_k = 2\pi\sigma_r\sigma_t S_k$. In fitting this model to the ψ - r image of the inner knot, we include a constant-surface-brightness background S_b as a model parameter.

While this simple model provides adequate estimates to characterize the primary properties of the knot (Table 6), as a check we also introduced a somewhat more complicated model to deal with minor asymmetries in the ψ - r plane. In particular, we took the radial location and radial width to be weak functions of the azimuthal angle, which we expand as a Taylor series to second order: $r \approx r(\psi) \approx r_0 + r'_0(\psi - \psi_0) + \frac{1}{2}r''_0(\psi - \psi_0)^2$ and $\sigma_r \approx \sigma_r(\psi) \approx \sigma_{r_0} + \sigma'_{r_0}(\psi - \psi_0) + \frac{1}{2}\sigma''_{r_0}(\psi - \psi_0)^2$. However, the derivatives proved not to alter significantly the results.

Comparison between methods

The comparison between methods and the reasons for somewhat emphasizing the SVD-based results considers the various measured parameters individually. Figure 14 compares measurements of similar variables between the two methods and illustrates the fact that the two methods. From the figure we see that, with the possible exception of the knot flux, both methods yield measurements that track each other apart from a scale factor. This leads to the result that the pulsar–knot separation determines all the intrinsic properties of the knot.

Differences for r_0 are quite small, whereas the knot flux and size estimates differ by factors of ≈ 2 . We would expect differences in the size estimates as the two analyses are using different measures of knot size—the first, RMS full width (FWRMS); the second, FWHM—which are not simply related for a non-Gaussian profile. That the fluxes differ is not perhaps so surprising as its measurement is sensitive to the method of background subtraction and the impact of emission in the wings of the inner knot’s profile. A significant difference between the two methods is the smaller uncertainty in r_0 afforded by the SVD approach, which removes those SVD components that represent noise, thus enhancing signal to noise.

A.3. *Chandra*

Figure 5 shows the summed image at pulse minimum from the 6 “flaring” observations (ObsIDs 14684-16247 in Table 3). Prior to the binning used to produce the figure, we extract the counts in the 3 regions shown. It is difficult, if not impossible, to make use of the absolute number of counts as the different instrument configurations are all uncalibrated. However, we can make use of the relative numbers of counts from the different regions. Thus, the central region serves as an indicator of the number of pulsar counts which can then be compared with the other observations to derive physical fluxes (assuming of course that the phase averaged pulsar flux has not varied). The region to the southeast provides the upper limit for the flux in the knot and we use the region to the northwest to estimate the background, comprised mainly of that due to the wings of the pulsar PSF.

The alert reader will notice a slight excess of counts roughly $0.6''$ to the southwest of the pulsar. This feature is seen both in the phase-averaged pulse and in the data from ObsID 11245. (The asymmetric effect of the blade inserted for Obs ID 9765 does not allow these data to be used in making this comparison.) Therefore, we conclude that this feature is part of the pulsar PSF. A more subtle effect is also present as there is a slight asymmetry in the PSF that causes the region we associate with the inner knot to be somewhat brighter than the background during observations taken in the fall. In the spring, when the spacecraft has (naturally) been set at a roll angle that differs by ≈ 180 deg from that in the fall, the background region is brighter than that we associate with the location of the inner knot. This effect is mainly seen in the phase averaged data, and by comparing data from the ObsID 9765 (spring) and ObsID 11245 (fall) observations. Both effects described in this paragraph are relatively minor, are mainly due to the fact we are working slightly below the spatial resolution of *Chandra*, and have thus been ignored in setting the upper limits in Table 8

REFERENCES

- H. E. S. S. Collaboration, Abramowski, A., Aharonian, F., et al. 2014, *A&A*, 562, LL4
- Aliu, E., Archambault, S., Aune, T., et al. 2014, *ApJ*, 781, LL11
- Arons, J. 2012, *Space Sci. Rev.*, 173, 341
- Baty, H., Petri, J., & Zenitani, S. 2013, *MNRAS*, 436, L20
- Beckwith, S. V. W., Stiavelli, M., Koekemoer, A. M., et al. 2006, *AJ*, 132, 1729
- Bertin, E., & Arnouts, S. 1996, *A&AS*, 117, 393

- Bogovalov, S. V. 1999, *A&A*, 349, 1017
- Bühler, R., & Blandford, R. 2014, *Reports on Progress in Physics*, 77, 066901
- Buehler, R., Scargle, J. D., Blandford, R. D., et al. 2012, *ApJ*, 749, 26
- Buson, S., Buehler, R., & Hays, E. 2013, *The Astronomer’s Telegram*, 5485, 1
- Bykov, A. M., Pavlov, G. G., Artemyev, A. V., & Uvarov, Y. A. 2012, *MNRAS*, 421, L67
- Camus, N. F., Komissarov, S. S., Bucciantini, N., & Hughes, P. A. 2009, *MNRAS*, 400, 1241
- Cerutti, B., Uzdensky, D. A., & Begelman, M. C. 2012, *ApJ*, 746, 148
- Cerutti, B., Werner, G. R., Uzdensky, D. A., & Begelman, M. C. 2013, *ApJ*, 770, 147
- Clausen-Brown, E., & Lyutikov, M. 2012, *MNRAS*, 426, 1374
- Fitzpatrick, E. L. 1999, *PASP*, 111, 63
- Fruchter, A. S., & Hook, R. N. 2002, *PASP*, 114, 144
- Ghez, A. M., Salim, S., Weinberg, N. N., et al. 2008, *ApJ*, 689, 1044
- Hester, J. J. 2008, *ARA&A*, 46, 127
- Hester, J. J., Scowen, P. A., Sankrit, R., et al. 1995, *ApJ*, 448, 240
- Komissarov, S. S., & Lyubarsky, Y. E. 2003, *MNRAS*, 344, L93
- Komissarov, S. S., & Lyutikov, M. 2011, *MNRAS*, 414, 2017
- Kron, R. G. 1980, *ApJS*, 43, 305
- Lind, K. R., & Blandford, R. D. 1985, *ApJ*, 295, 358
- Lyubarsky, Y. E. 2012, *MNRAS*, 427, 1497
- Lyutikov, M., Balsara, D., & Matthews, C. 2012, *MNRAS*, 422, 3118
- Lyutikov, M., Pariev, V. I., & Blandford, R. D. 2003, *ApJ*, 597, 998
- Mayer, M., Buehler, R., Hays, E., et al. 2013, *ApJ*, 775, L37
- Melatos, A., Scheltus, D., Whiting, M. T., Eikenberry, S. S., Romani, R. W., Rigaut, F., Spitkovsky, A., Arons, J. & Payne, D. J. B. 2005, *ApJ*, 633, 931

- Moran, P., Shearer, A., Mignani, R. P., Słowikowska, A., De Luca, A., Gouiffès, C., & Laurent, P. 2013, MNRAS, 433, 2564
- Ng, C.-Y. & Romani, R. W. 2008, ApJ, 673, 411
- Ojha, R., Hays, E., Buehler, R., & Dutka, M. 2013, The Astronomer's Telegram, 4855, 1
- Porth, O., Komissarov, S. S., & Keppens, R. 2014, MNRAS, 438, 278
- Rees, M. J., & Gunn, J. E. 1974, MNRAS, 167, 1
- Sandberg, A., & Sollerman, J. 2009, A&A, 504, 525
- Sollerman, J., Lundqvist, P., Lindler, D., Chevalier, R. A., Fransson, C., Gull, T. R., Pun, C. S. J., & Sonneborn, G. 2000, ApJ, 537, 861
- Sollerman, J. 2003, A&A, 406, 639
- Spitkovsky, A. 2006, ApJ, 648, L51
- Striani, E., Tavani, M., Piano, G., et al. 2011, ApJ, 741, L5
- Sturrock, P., & Aschwanden, M. J. 2012, ApJ, 751, L32
- Tavani, M., Bulgarelli, A., Vittorini, V., et al. 2011, Science, 331, 736
- Tennant, A. F., Becker, W., Juda, M., et al. 2001, ApJ, 554, L173
- Tchekhovskoy, A., Spitkovsky, A., & Li, J. G. 2013, MNRAS, 435, L1
- Tchekhovskoy, A., Philippov, A. & Spitkovsky, A. 2015, eprint arXiv:1503.01467
- Teraki, Y., & Takahara, F. 2013, ApJ, 763, 131
- Tziamtzis, A., Lundqvist, P., & Djupvik, A. A. 2009, A&A, 508, 221
- Uzdensky, D. A., Cerutti, B., & Begelman, M. C. 2011, ApJ, 737, L40
- Wizinowich, P. L., Le Mignant, D., Bouchez, A. H., Campbell, R. D., Chin, J. C. Y. et al. 2006, PASP, 118, 297
- Weisskopf, M. C., Tennant, A. F., Arons, J., et al. 2013, ApJ, 765, 56
- Yuan, Q., Yin, P.-F., Wu, X.-F., Bi, X.-J., Liu, S., & Zhang, B. 2011, ApJ, 730, L15
- Yelda, S., Lu, J. R., Ghez, A. M., et al. 2010, ApJ, 725, 331

Table 1: Summary of the Keck observations

#	Date	MJD ^a	Instrument ^b	Exposure (s)
K1	2012-02-08	55965.285	NIRC2-wide	420
K2	2012-03-05	55991.319	NIRC2-wide	420
K3	2012-12-22	56283.408	NIRC2-wide	1250
K4	2012-12-23	56284.410	NIRC2-narrow	870
K5	2012-12-24	56285.388	NIRC2-narrow	1350
K6	2012-12-25	56286.390	NIRC2-wide	1125
K7	2013-02-06	56329.308	NIRC2-narrow	2020
K8	2013-10-22	56587.448	NIRC2-narrow	640
K9	2014-01-09	56666.274	NIRC2-wide	1560
K10	2014-01-09	56666.377	NIRC2-narrow	2580
K11	2014-01-17	56674.325	NIRC2-wide	2270
K12	2014-01-17	56674.394	NIRC2-narrow	1260

^a Quoted MJD is at the midpoint of the observation.

^b Plate scale is 0.04"/pixel for NIRC2-wide; 0.01"/pixel for NIRC2-narrow.

Table 2: Summary of the HST observations

#	Date	MJD ^{ab}
H1	2012-01-08	55934.797
H2	2012-02-10	55967.170
H3	2012-03-12	55998.414
H4	2012-04-22	56039.850
H5	2012-08-16	56155.336
H6	2012-09-10	56180.960
H7	2013-01-10	56302.992
H8	2013-02-24	56347.055
H9	2013-03-06	56357.023
H10	2013-04-01	56383.320
H11	2013-04-14	56396.113
H12	2013-08-13	56517.710
H13	2013-10-20	56585.793
H14	2013-10-29	56594.700
H15	2013-12-01	56627.273
H16	2014-01-20	56677.530
H17	2014-04-13	56760.900

^a Quoted MJD is at the midpoint of the observation.

^b Plate scale is 0.05"/pixel.

Table 3: Summary of the *Chandra* observations

#	ObsID	Date	MJD ^a	Exposure (s)
C1	09765	2008-01-22	54487.670	95082
C2	11245	2010-11-16	55516.294	22039
C3	14684	2013-03-05	56356.972	19485
C4	14686	2013-03-10	56361.338	20052
C5	14687	2013-03-17	56368.324	16718
C6	16244	2013-10-19	56584.658	20048
C7	16246	2013-10-22	56587.515	20013
C8	16247	2013-10-24	56589.007	19770

^a Quoted MJD is at the start of the observation.

Table 4: Knot properties based upon analysis of the Keck data

#	ψ_0 °	r_0 "	FWHM _r "	FWHM _t "	F_k F_p
K1	118.50 ± 0.16	0.6711 ± 0.0015	0.3931 ± 0.0040	0.4719 ± 0.0051	0.0639 ± 0.0045
K2	121.00 ± 0.13	0.6577 ± 0.0015	0.4121 ± 0.0035	0.4252 ± 0.0042	0.0626 ± 0.0067
K3	122.64 ± 0.11	0.6893 ± 0.0011	0.3215 ± 0.0028	0.3948 ± 0.0039	0.0804 ± 0.0074
K4	120.96 ± 0.18	0.7118 ± 0.0021	0.3401 ± 0.0051	0.4081 ± 0.0059	0.0473 ± 0.0003
K5	121.20 ± 0.07	0.6981 ± 0.0007	0.2983 ± 0.0019	0.3767 ± 0.0024	0.0555 ± 0.0005
K6	120.79 ± 0.12	0.7164 ± 0.0010	0.3375 ± 0.0029	0.4238 ± 0.0042	0.0599 ± 0.0085
K7	121.93 ± 0.12	0.7756 ± 0.0013	0.3355 ± 0.0034	0.4049 ± 0.0038	0.0662 ± 0.0004
K8	120.33 ± 0.06	0.5722 ± 0.0004	0.2216 ± 0.0011	0.3172 ± 0.0015	0.0621 ± 0.0005
K9	121.46 ± 0.08	0.6543 ± 0.0006	0.2958 ± 0.0018	0.4030 ± 0.0024	0.0708 ± 0.0047
K10	115.77 ± 0.03	0.6257 ± 0.0003	0.2689 ± 0.0007	0.3683 ± 0.0009	0.0663 ± 0.0006
K11	121.49 ± 0.10	0.6371 ± 0.0008	0.3119 ± 0.0022	0.3787 ± 0.0029	0.0647 ± 0.0078
K12	118.99 ± 0.09	0.6438 ± 0.0009	0.3248 ± 0.0023	0.3766 ± 0.0025	0.0574 ± 0.0001

Table 5: Results of regression analyses for the 12 Keck observations

Power-law for $r_1 = 0.6692''$				
Property	Unit	$p(r_1)$	Power-law index q	Probability
FWHM_r	"	0.3180 ± 0.0132	1.19 ± 0.54	5.4E-2
FWHM_t	"	0.3941 ± 0.0093	0.75 ± 0.31	3.8E-2
S_k	$F_p/('')^2$	0.439 ± 0.033	-2.14 ± 0.97	5.2E-2
F_k	F_p	0.0626 ± 0.0025	-0.20 ± 0.53	7.1E-1
Linear for $\langle r_0 \rangle = 0.6711''$				
Property		$\psi_0(\langle r_0 \rangle)$	$d\psi_0/dr_0$	
ψ_0	$^\circ, \text{ }^\circ/''$	120.42 ± 0.51	15.2 ± 10.2	1.7E-1

Table 6: Knot properties based upon SVD analysis of the 17 HST observations (see Appendix)

#	ψ_0 °	r_0 ''	FWHM_r ''	FWHM_t ''	S_k $e/s/('')^2$	F_k e/s	F_p e/s	F_k F_p
H1	120.54 ± 0.40	0.6819 ± 0.0023	0.1526 ± 0.0056	0.3221 ± 0.0116	1064 ± 33	59.8 ± 3.6	1425 ± 82	0.0420 ± 0.0035
H2	119.45 ± 0.41	0.6535 ± 0.0024	0.1536 ± 0.0058	0.3071 ± 0.0114	1008 ± 32	53.8 ± 3.4	1433 ± 80	0.0375 ± 0.0032
H3	120.37 ± 0.33	0.6708 ± 0.0022	0.1751 ± 0.0052	0.3121 ± 0.0092	902 ± 23	55.0 ± 2.6	1471 ± 64	0.0374 ± 0.0024
H4	121.74 ± 0.41	0.6356 ± 0.0024	0.1465 ± 0.0056	0.2942 ± 0.0110	1053 ± 34	52.3 ± 3.2	1276 ± 80	0.0410 ± 0.0035
H5	117.90 ± 0.39	0.6166 ± 0.0020	0.1406 ± 0.0048	0.3043 ± 0.0102	1256 ± 36	61.1 ± 3.4	1231 ± 84	0.0497 ± 0.0044
H6	117.62 ± 0.41	0.6577 ± 0.0024	0.1456 ± 0.0058	0.3029 ± 0.0112	1102 ± 36	56.7 ± 3.5	1184 ± 86	0.0479 ± 0.0046
H7	121.17 ± 0.59	0.7240 ± 0.0035	0.1704 ± 0.0084	0.3539 ± 0.0176	675 ± 28	44.7 ± 3.9	1422 ± 77	0.0314 ± 0.0032
H8	119.91 ± 0.50	0.7516 ± 0.0031	0.1751 ± 0.0076	0.3533 ± 0.0158	667 ± 25	44.5 ± 3.4	1421 ± 65	0.0313 ± 0.0028
H9	120.88 ± 0.52	0.7491 ± 0.0033	0.1740 ± 0.0080	0.3362 ± 0.0166	728 ± 29	45.8 ± 3.8	1359 ± 73	0.0337 ± 0.0033
H10	120.60 ± 0.32	0.6614 ± 0.0019	0.1598 ± 0.0046	0.3139 ± 0.0090	1098 ± 27	63.3 ± 3.0	1295 ± 72	0.0489 ± 0.0036
H11	119.39 ± 0.36	0.6557 ± 0.0021	0.1639 ± 0.0050	0.3220 ± 0.0098	1090 ± 28	64.9 ± 3.3	1509 ± 77	0.0430 ± 0.0031
H12	119.28 ± 0.41	0.6324 ± 0.0023	0.1691 ± 0.0056	0.3299 ± 0.0110	1028 ± 29	63.4 ± 3.6	1283 ± 83	0.0494 ± 0.0042
H13	117.85 ± 0.36	0.5687 ± 0.0019	0.1426 ± 0.0046	0.2739 ± 0.0082	1668 ± 44	75.6 ± 3.8	1222 ± 106	0.0618 ± 0.0062
H14	118.82 ± 0.41	0.5849 ± 0.0022	0.1441 ± 0.0052	0.2886 ± 0.0098	1583 ± 48	75.6 ± 4.4	1285 ± 118	0.0589 ± 0.0064
H15	118.59 ± 0.52	0.6624 ± 0.0026	0.1476 ± 0.0061	0.3393 ± 0.0144	1105 ± 40	61.8 ± 4.4	1353 ± 100	0.0457 ± 0.0047
H16	118.82 ± 0.41	0.6299 ± 0.0026	0.1640 ± 0.0064	0.2961 ± 0.0106	1084 ± 35	62.1 ± 3.7	1419 ± 98	0.0438 ± 0.0040
H17	120.88 ± 0.41	0.6448 ± 0.0024	0.1611 ± 0.0058	0.3212 ± 0.0110	1164 ± 35	69.6 ± 4.0	1177 ± 99	0.0591 ± 0.0060

Table 7: Results of regression analyses for the 17 HST observations based on the data in Table 6

Power-law for $r_1 = 0.6559''$				
Property	Unit	$p(r_1)$	Power-law index q	Probability
FWHM _r	"	0.1575 ± 0.0022	0.72 ± 0.19	1.7E-3
FWHM _t	"	0.3152 ± 0.0029	0.80 ± 0.13	1.4E-5
S_k	$F_p/('')^2$	0.782 ± 0.023	-3.66 ± 0.40	1.7E-7
F_k	F_p	0.0440 ± 0.0012	-2.39 ± 0.37	9.8E-6
Linear for $\langle r_0 \rangle = 0.6577''$				
Property		$\psi_0(\langle r_0 \rangle)$	$d\psi_0/dr_0$	
ψ_0	$^\circ, \text{ }^\circ/''$	119.64 ± 0.27	13.5 ± 5.5	2.7E-2

Table 8: Results of the *Chandra* analysis

ObsID	Pulse Average			Pulse Minimum			F_k/F_p
	Pulsar	Knot	Background	Pulsar	Knot	Background	3σ
09765	51844	2963	3704	845	57	72	< 0.0022
11245	5630	1018	851	88	16	12	< 0.0094
last 6	13549	2622	2503	203	39	44	< 0.0067

Table 9: *Fermi*/LAT 12-hr-average fluxes and pulsar–knot separations as measured with Keck and HST (SVD analysis)

#	Date	t_{mid} MJD	r_0 "	<i>Fermi</i> /LAT ≥ 100 MeV 10^{-6} ph/s/cm ²
H1	2012-01-08	55934.797	0.6819 ± 0.0023	2.45 (+0.47, -0.43)
K1	2012-02-08	55965.280	0.6711 ± 0.0015	2.58 (+0.60, -0.54)
H2	2012-02-10	55967.171	0.6535 ± 0.0024	2.79 (+0.65, -0.58)
K2	2012-03-05	55991.311	0.6577 ± 0.0015	2.78 (+0.46, -0.43)
H3	2012-03-12	55998.414	0.6708 ± 0.0022	3.55 (+0.52, -0.49)
H4	2012-04-22	56039.850	0.6356 ± 0.0024	2.18 (+0.56, -0.50)
H5	2012-08-16	56155.336	0.6166 ± 0.0020	3.25 (+0.56, -0.52)
H6	2012-09-10	56180.960	0.6577 ± 0.0024	3.86 (+0.50, -0.47)
K3	2012-12-22	56283.381	0.6893 ± 0.0011	3.13 (+0.68, -0.63)
K4	2012-12-23	56284.403	0.7118 ± 0.0021	3.51 (+0.67, -0.62)
K5	2012-12-24	56285.379	0.6981 ± 0.0007	3.29 (+0.67, -0.62)
K6	2012-12-25	56286.370	0.7164 ± 0.0010	2.74 (+0.62, -0.56)
H7	2013-01-10	56302.992	0.7240 ± 0.0035	3.22 (+0.66, -0.66)
K7	2013-02-06	56329.248	0.7756 ± 0.0013	3.93 (+0.75, -0.70)
H8	2013-02-24	56347.055	0.7516 ± 0.0031	5.44 (+0.72, -0.68)
H9	2013-03-06	56357.023	0.7491 ± 0.0033	10.09 (+0.52, -0.51)
H10	2013-04-01	56383.320	0.6614 ± 0.0019	3.50 (+0.68, -0.63)
H11	2013-04-14	56396.113	0.6557 ± 0.0021	2.89 (+0.59, -0.54)
H12	2013-08-13	56517.710	0.6324 ± 0.0023	2.65 (+0.46, -0.43)
H13	2013-10-20	56585.793	0.5687 ± 0.0019	3.71 (+0.26, -0.25)
K8	2013-10-22	56587.443	0.5722 ± 0.0004	1.25 (+1.73, -1.73)
H14	2013-10-29	56594.700	0.5849 ± 0.0022	7.46 (+1.16, -1.07)
H15	2013-12-01	56627.273	0.6624 ± 0.0026	2.15 (+0.53, -0.47)
K9	2014-01-09	56666.316	0.6543 ± 0.0006	3.38 (+0.53, -0.50)
K10	2014-01-09	56666.438	0.6257 ± 0.0003	3.54 (+0.51, -0.48)
K11	2014-01-17	56674.356	0.6371 ± 0.0008	3.84 (+0.53, -0.50)
K12	2014-01-17	56674.400	0.6438 ± 0.0009	3.47 (+0.44, -0.42)
H16	2014-01-20	56677.530	0.6299 ± 0.0026	2.85 (+0.43, -0.41)
H17	2014-04-13	56760.900	0.6448 ± 0.0024	3.96 (+0.78, -0.71)

Table 10: Results of the Traditional HST Analysis

#	r_0 "	FWRMS $_r$ "	FWRMS $_t$ "	F_k e/s
H1	0.660 ± 0.012	0.287 ± 0.019	0.551 ± 0.037	116.5 ± 2.9
H2	0.634 ± 0.012	0.283 ± 0.020	0.538 ± 0.038	110.9 ± 2.8
H3	0.649 ± 0.013	0.333 ± 0.021	0.594 ± 0.038	131.6 ± 3.3
H4	0.615 ± 0.012	0.255 ± 0.020	0.489 ± 0.038	90.4 ± 2.3
H5	0.588 ± 0.012	0.278 ± 0.019	0.560 ± 0.038	112.9 ± 2.8
H6	0.635 ± 0.012	0.290 ± 0.020	0.552 ± 0.037	111.6 ± 2.8
H7	0.706 ± 0.010	0.288 ± 0.021	0.589 ± 0.044	97.6 ± 2.4
H8	0.734 ± 0.017	0.336 ± 0.024	0.658 ± 0.046	109.2 ± 2.7
H9	0.732 ± 0.013	0.319 ± 0.022	0.650 ± 0.046	108.1 ± 2.7
H10	0.641 ± 0.009	0.299 ± 0.020	0.580 ± 0.039	117.6 ± 2.9
H11	0.637 ± 0.011	0.314 ± 0.020	0.561 ± 0.036	129.2 ± 3.2
H12	0.613 ± 0.012	0.258 ± 0.017	0.578 ± 0.039	121.3 ± 3.0
H13	0.547 ± 0.009	0.224 ± 0.015	0.491 ± 0.033	119.2 ± 3.0
H14	0.552 ± 0.009	0.236 ± 0.015	0.511 ± 0.033	124.8 ± 3.1
H15	0.631 ± 0.012	0.268 ± 0.018	0.588 ± 0.040	115.2 ± 2.9
H16	0.614 ± 0.011	0.266 ± 0.025	0.519 ± 0.049	116.9 ± 2.9
H17	0.624 ± 0.012	0.259 ± 0.024	0.549 ± 0.050	127.8 ± 3.2

Table 11: Results of regression analyses for the 17 HST observations based on the traditional data analysis

Power-law for $r_1 = 0.6342''$				
Property	Unit	$p(r_1)$	Power-law index q	Probability
FWRMS $_r$	"	0.2801 ± 0.0046	1.14 ± 0.21	6.0E-5
FWRMS $_t$	"	0.5605 ± 0.0067	0.85 ± 0.15	4.9E-5
F_k	e/s	114.8 ± 2.6	-0.39 ± 0.29	1.9E-1

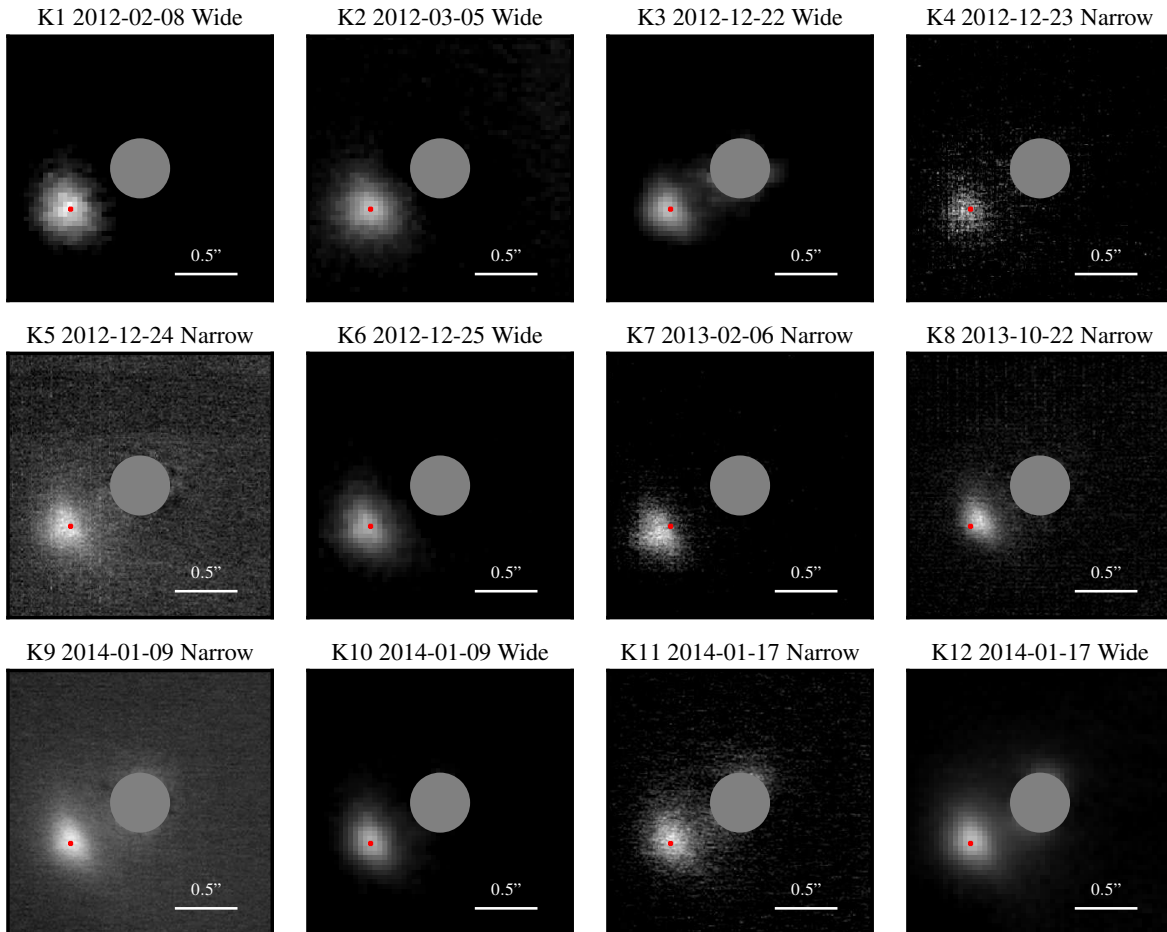


Fig. 1.— Individual images of the inner knot, with the pulsar removed, from Keck NIRC2 with laser-guide-star adaptive optics (AO). In each image, the PSF of the pulsar has been subtracted using the scaled PSF of a nearby star and replaced with a gray circle at the original location of the pulsar. Each image is $2.2''$ by $2.2''$. Images are from the NIRC2 wide camera ($0.04''$ pixels) or the NIRC2 narrow camera ($0.01''$ pixels). All images were taken using the K' filter. A red dot marks the average position of the inner knot across all 12 observations.

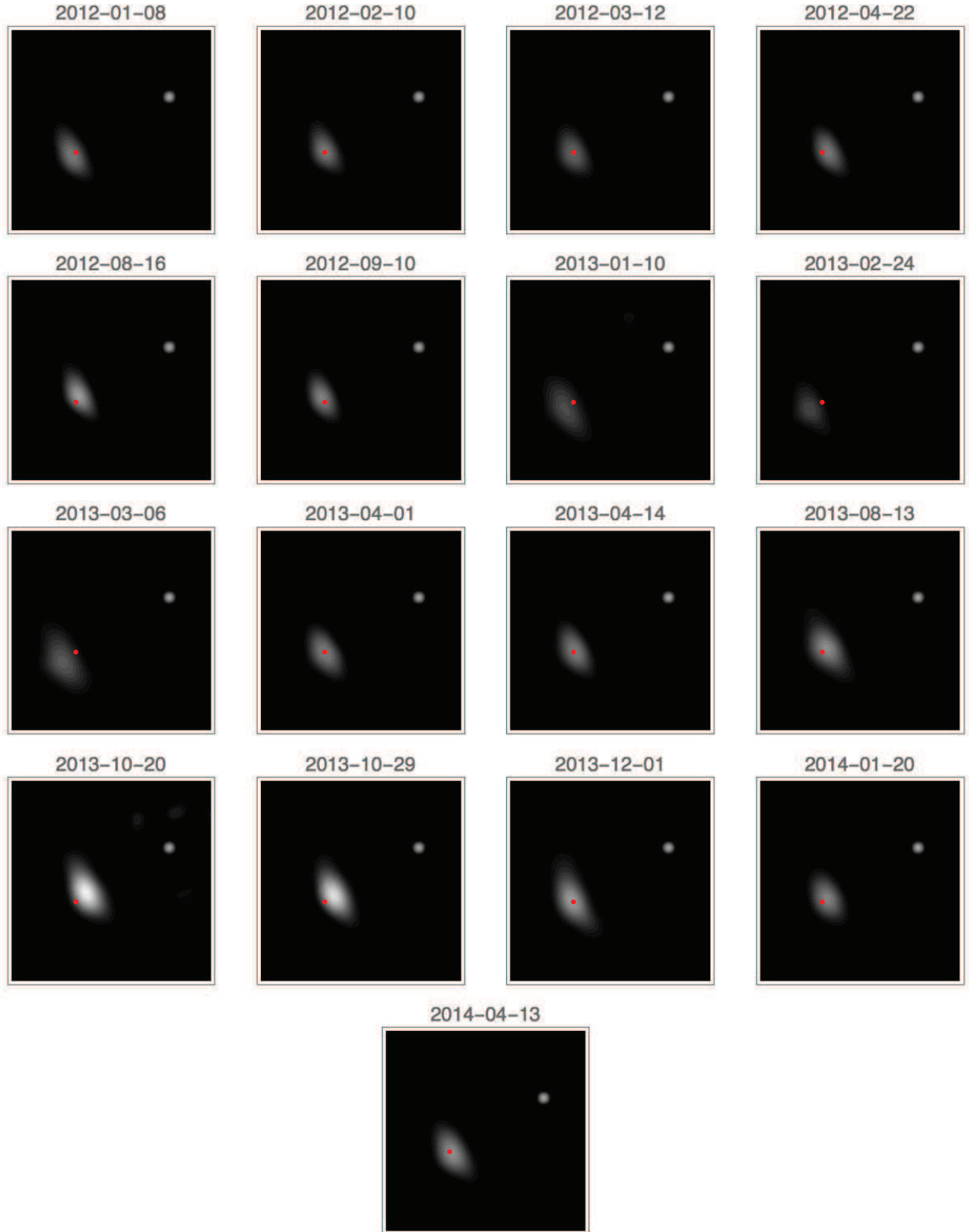


Fig. 2.— HST-SVD-Processed images of the Crab pulsar and inner knot after removing effects of the HST/ACS WFC point spread function. A red dot marks the average position of the inner knot across all 17 observations.

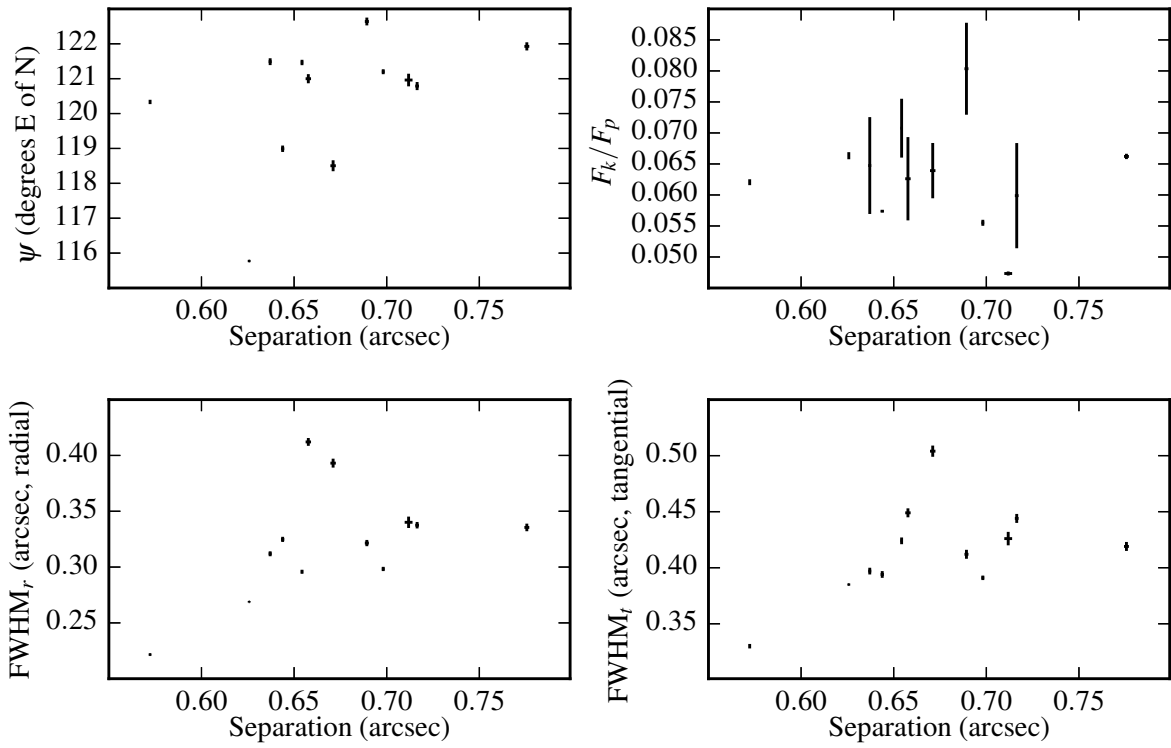


Fig. 3.— Variation of the Keck-measured knot properties versus separation of the inner knot from the pulsar.

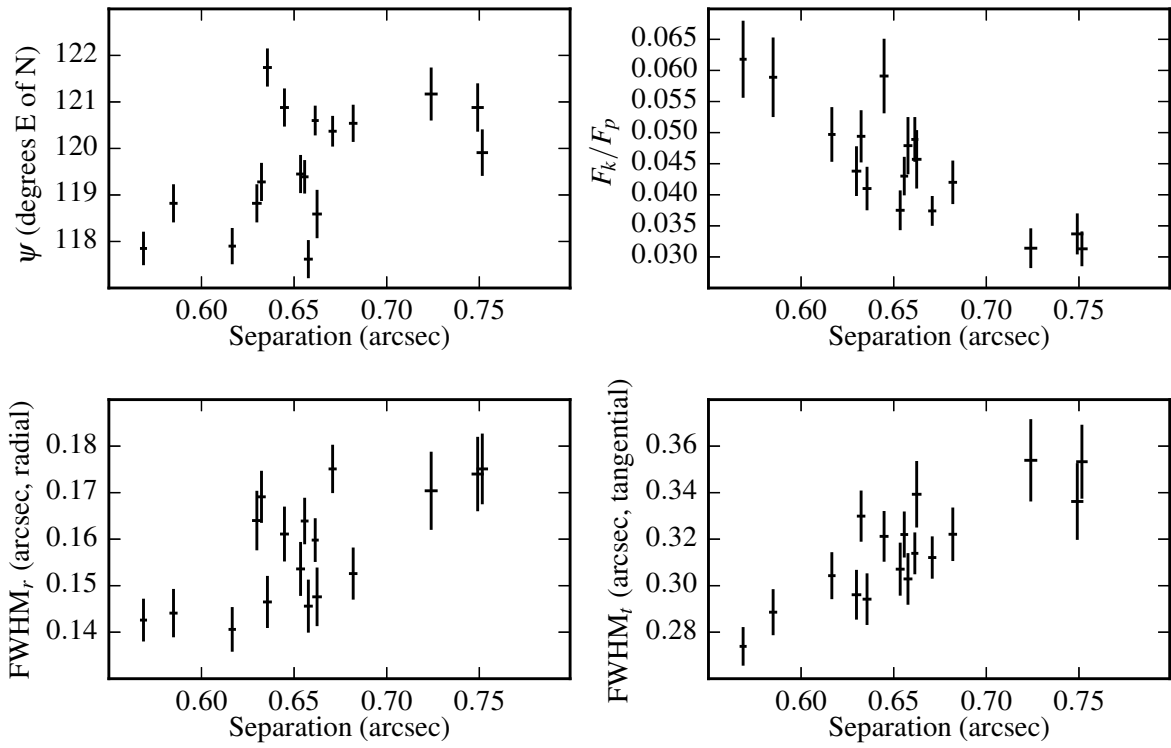


Fig. 4.— Variation of the HST-SVD-measured properties with separation of the inner knot from the pulsar.

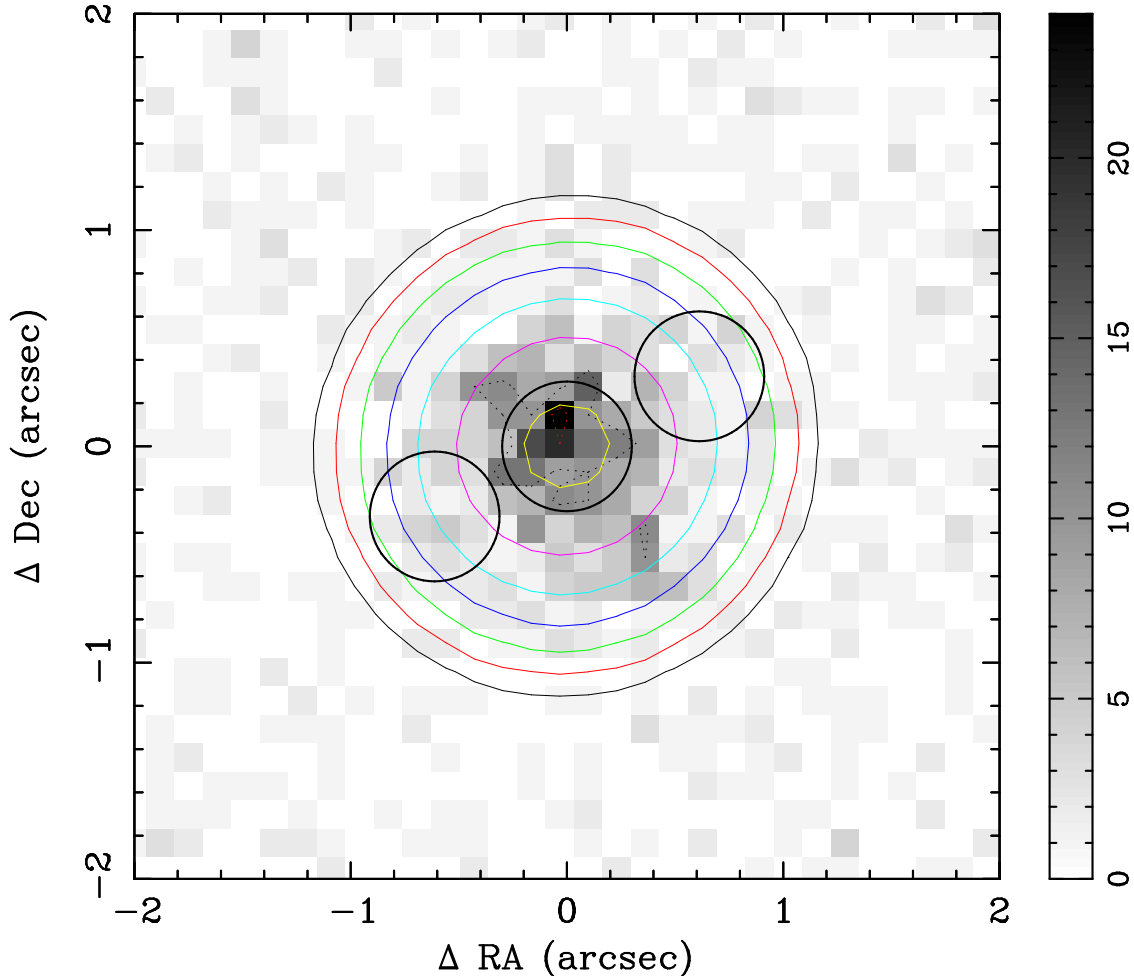


Fig. 5.— *Chandra* image at pulse minimum from the sum of the last 6 flaring data sets in Table 3. The 3 small black circles show $0.3''$ -radius extraction regions, the central of which is used to estimate the pulsar flux. The circle, at a position angle $\psi = 120^\circ$ east of north and $0.65''$ from the pulsar, is roughly centered on the average optical location of the knot. Data in the opposite small circle (the one to the NW where N is up) are used to estimate background. Large circles show the best-fit Gaussian to the phase-average pulsar data at intensity levels of 10, 20, 40, 80, 160, 320 and 640 cts/pixel illustrating the level of impact of the PSF at the site of the knot—i.e., slight but non-negligible. The intensity level is shown by the grayscale bar on the right.

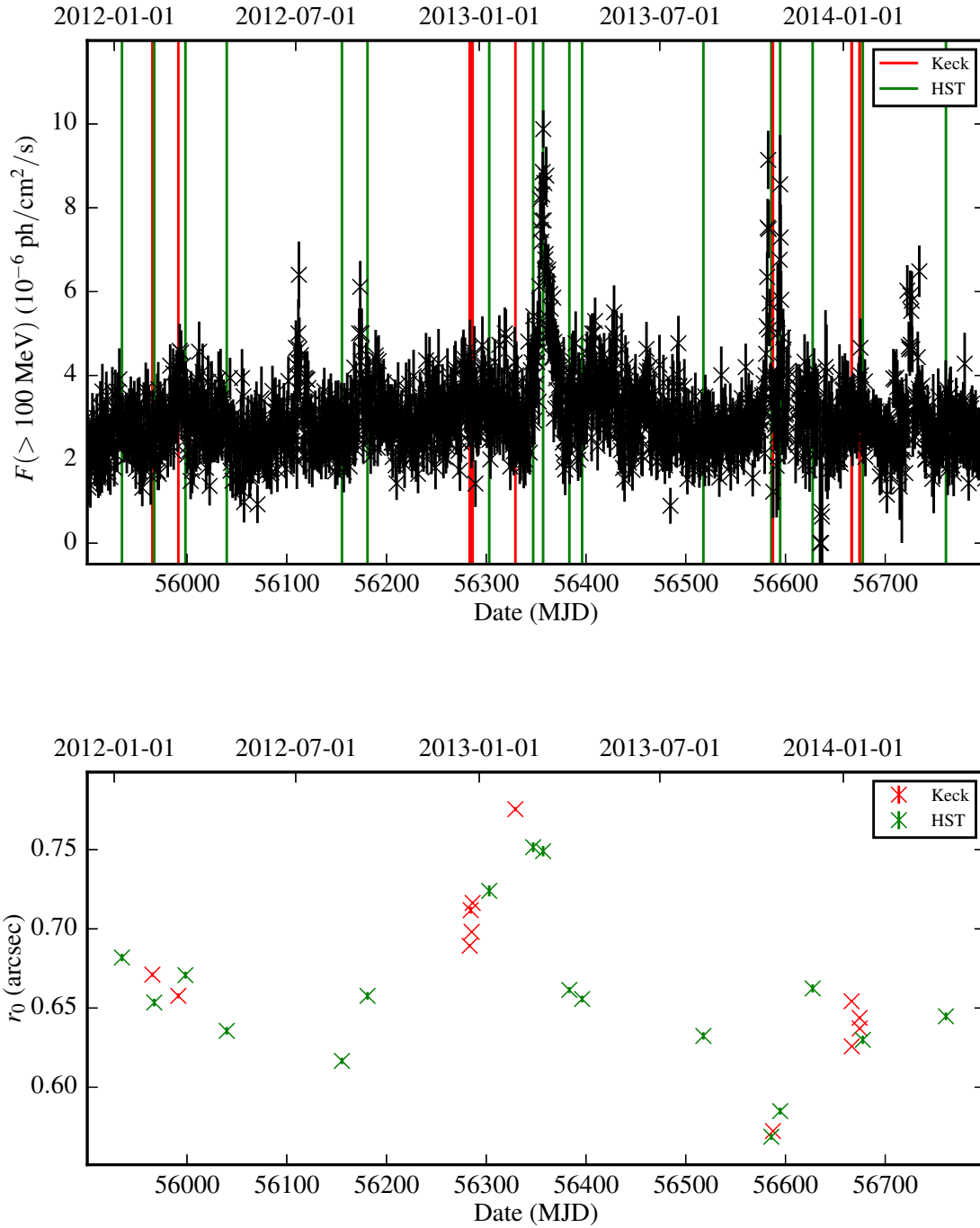


Fig. 6.— *Fermi*/LAT 12-hr average flux (upper panel) and pulsar-knot separation (lower panel) versus time, for Keck (red) and HST (green) observations.

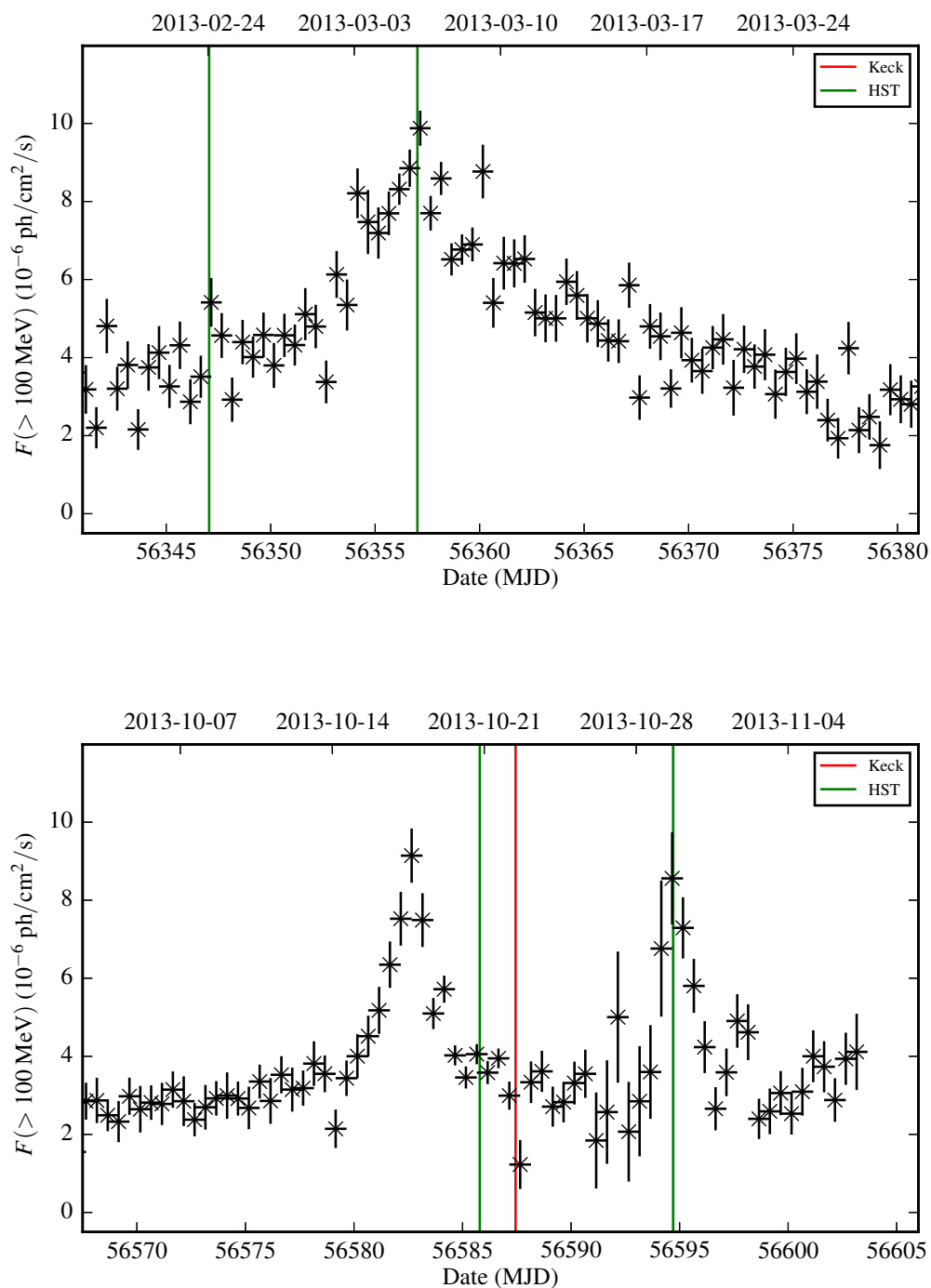


Fig. 7.— *Fermi*/LAT 12-hr average fluxes during Keck (red) and HST (green) observations at the time of the largest γ -ray flares in 2013 March (upper panel) and in 2013 October (lower panel).

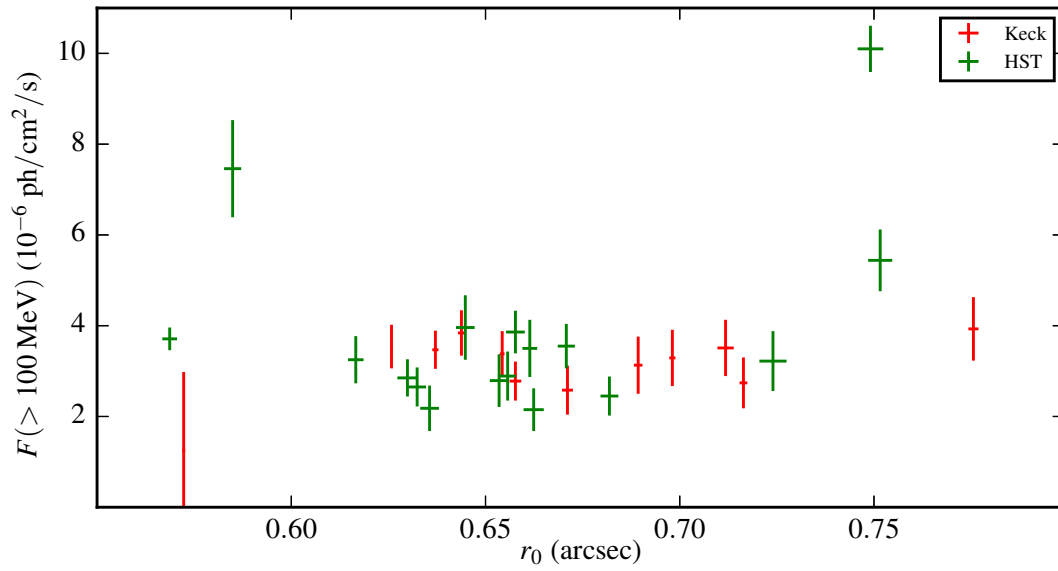


Fig. 8.— *Fermi*/LAT 12-hr-average fluxes centered on the times of Keck (red) and HST (green) measurements of pulsar–knot separations.

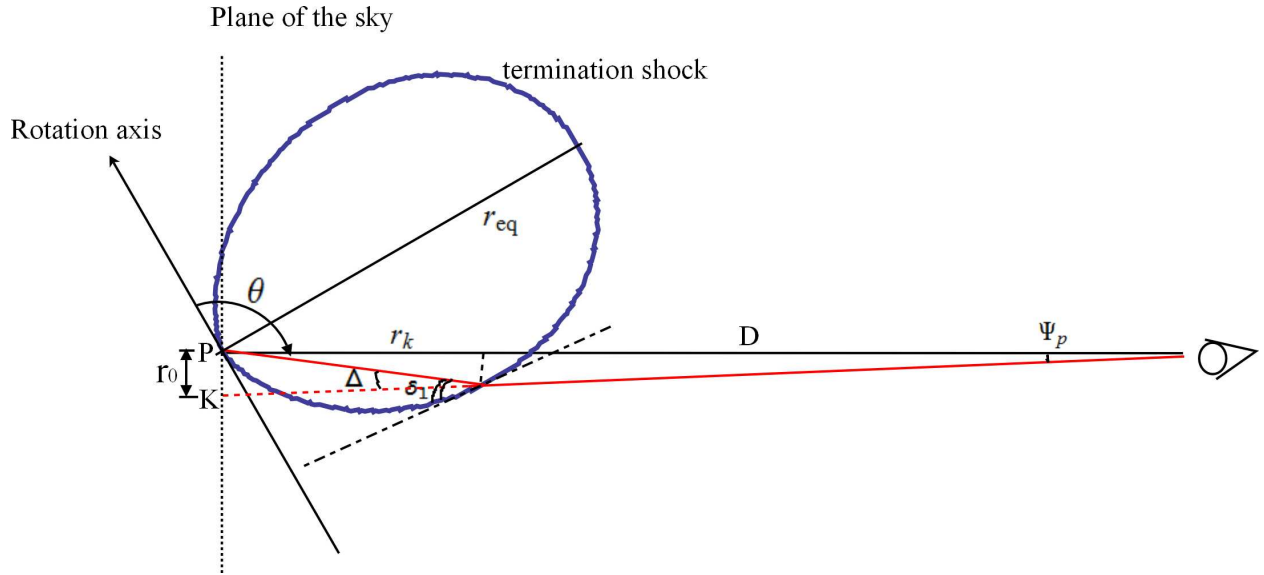


Fig. 9.— Geometry of the termination shock on the meridional plane determined by the pulsar rotation axis and the observer’s line of sight toward the pulsar. The pulsar is located at point P. The angle between line of sight and pulsar rotation axis is $\theta_{\text{ob}} = 2\pi/3$, consistent with that measured by Ng & Romani (2008). The knot is projected on the plane of the sky at an angle $r_0 \approx 0.65''$ southeast of the pulsar (represented by point K here). The angle between the upstream velocity and the shock surface is δ_1 . The outflow is deflected from the radial direction by an angle Δ .

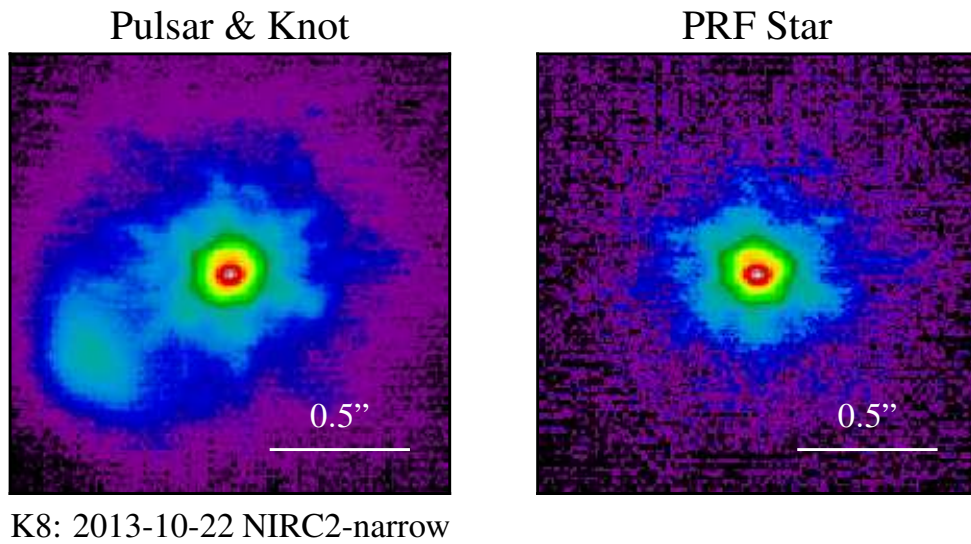


Fig. 10.— The Pulsar (left) and a nearby star (right) from Keck data taken on 2013 October 22. (a) An H filter image of the pulsar and knot (in the lower-left) as seen by the NIRC2-narrow camera (0.01'' pixels and a 10'' \times 10'' field of view). The structure of the knot is resolved and separated from the pulsar by a statistically significant valley. (b) A nearby (5'') comparison star, used to establish the point-response-function. Both images are shown with a logarithmic color stretch.

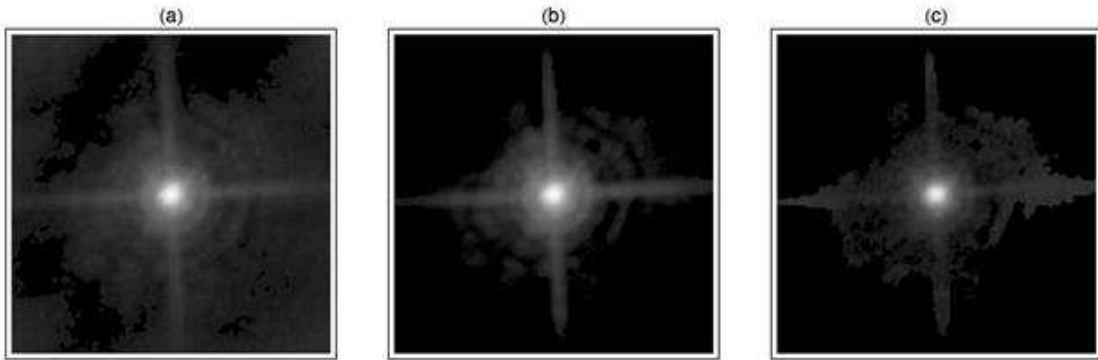


Fig. 11.— Images illustrating the steps in determining the HST/ACS PSF for this analysis: (a) Extract 323 (19×17) 121×121 -pixel ($6.05'' \times 6.05''$) images and subtract a linear-gradient background for 19 isolated stars in these 17 HST/ACS observations of the Crab; (b) register images of stars and use singular value decomposition (SVD) to determine a basis describing the PSF (first SVD component shown); and (c) model the pulsar image using the first 72 SVD components.

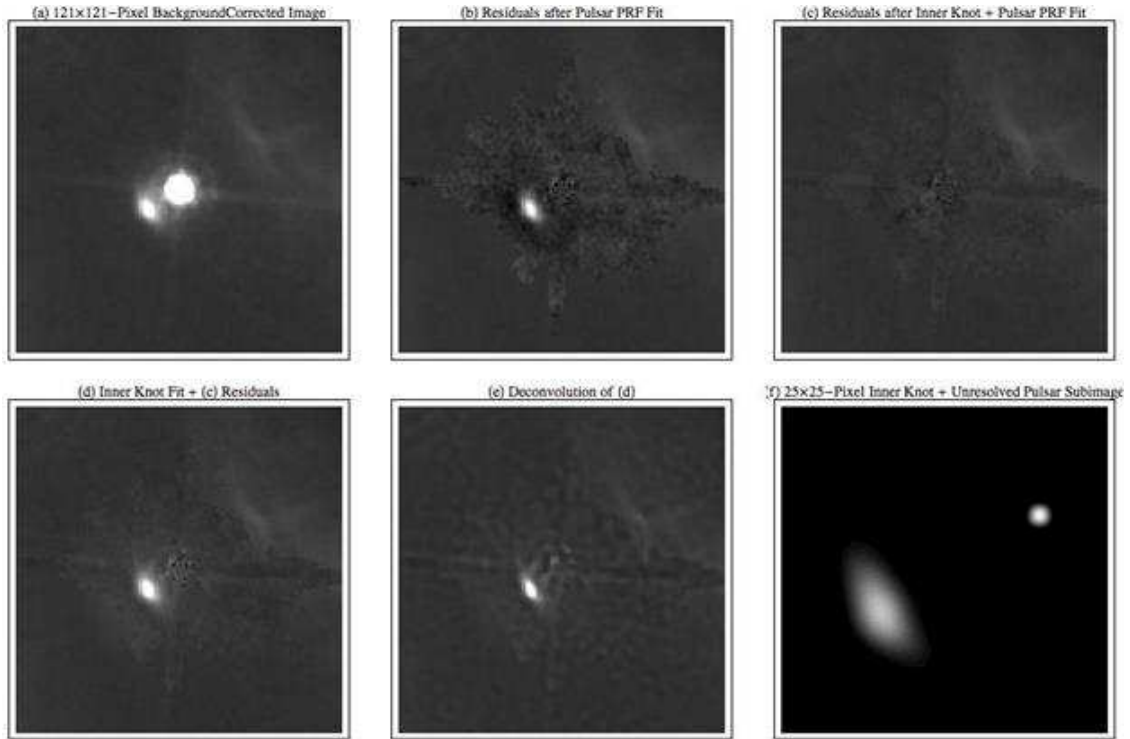


Fig. 12.— Images further illustrating steps in processing HST/ACS images of the Crab pulsar and inner knot: (a) Subtract a linear-gradient background in central 121×121 pixel ($6.05'' \times 6.05''$) image of pulsar and inner knot; (b) remove pulsar using SVD model of PSF leaving inner knot; (c) remove inner knot using its SVD model leaving residual background; (d) add SVD model of inner knot to residual background; (e) apply Richardson-Lucy algorithm to generate deconvolved image of inner knot (and residual background); and (f) synthesize 25×25 pixel ($1.25'' \times 1.25''$) sub-image of registered (unresolved) pulsar and SVD model of inner knot.

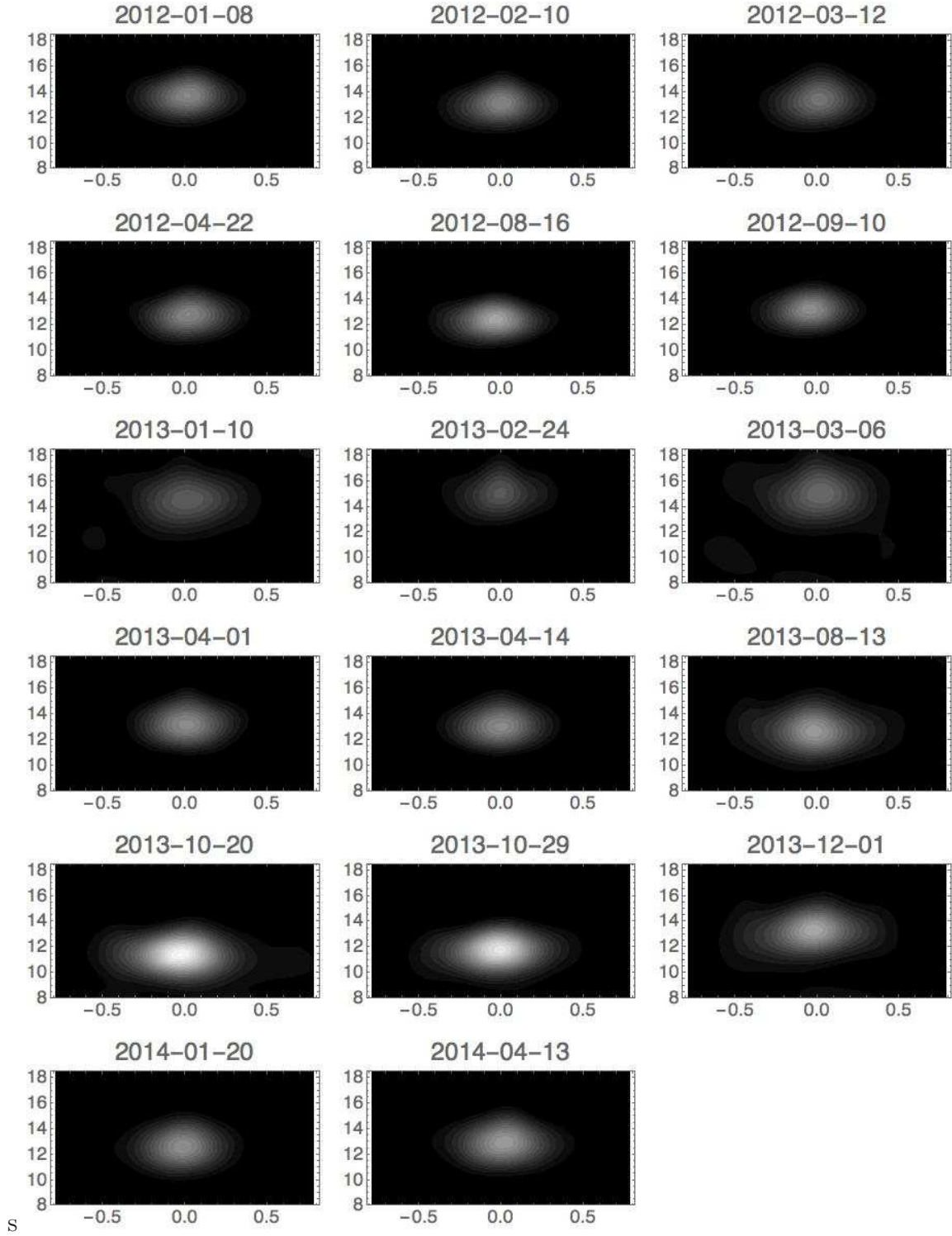


Fig. 13.— Mapping of processed images of the inner knot onto a ψ - r grid. Here ψ is the angular displacement in radian from the knot's centroid; r , the radial distance from the pulsar in ($0.05''$) pixels.

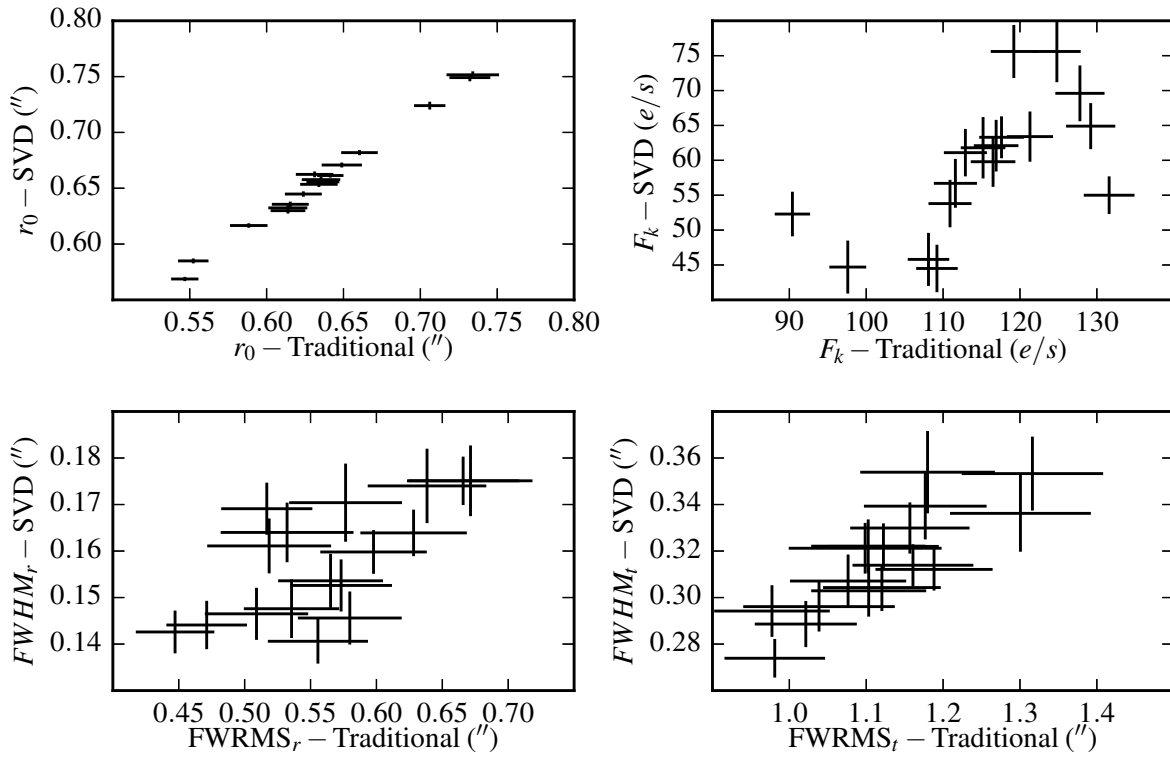


Fig. 14.— Comparison of HST-SVD and HST-traditional measured properties of the inner knot.